Archives of Biochemistry and Biophysics 775 (2026) 110675

Contents lists available at ScienceDirect

Archives of Biochemistry and Biophysics

journal homepage: www.elsevier.com/locate/yabbi

Altered dimerization of certain riboflavin transporter 2 mutants: a possible source of UPR, altered calcium signalling and mitochondrial derangements in RTD2

Maria Tolomeo [a], Valentina Magliocca [b,c,1], Stefania Petrini [d,1], Alessia Nisco [e], Roberto Barbaro [e], Martina Lanza [e], Michela Piccione [d], Anna Maria Giudetti [f], Keith Massey [g], Lara Console [h], Cesare Indiveri [a,h], Katia Zanier [i], Enrico Bertini [j], Tiziana Persichini [c], Claudia Compagnucci [b], Matilde Colella [e], Maria Barile [e,*]

[a] CNR Institute of Biomembranes, Bioenergetics and Molecular Biotechnology, Bari, Italy
[b] Molecular Genetics and Functional Genomics, Ospedale Pediatrico Bambino Gesù, IRCCS, Rome, Italy
[c] Department of Science, University "Roma Tre", Rome, Italy
[d] Confocal Microscopy Core Facility, Research Laboratories, Bambino Gesù Children's Hospital, IRCCS, Rome, Italy
[e] Department of Biosciences, Biotechnologies, and Environment, University of Bari Aldo Moro, Bari, Italy
[f] Department of Biological and Environmental Sciences and Technologies (Di.S.Te.B.A.), University of Salento, Lecce, Italy
[g] Cure RTD Foundation, Calgary, AB, Canada
[h] Department DiBEST (Biologia, Ecologia e Scienze della Terra), University of Calabria, Arcavacata di Rende, Italy
[i] Biotechnology and Cell Signaling (CNRS/Université de Strasbourg, UMR 7242), Ecole Superieure de Biotechnologie de Strasbourg, Illkirch, France
[j] Unit of Neuromuscular and Neurodegenerative Disorders, Translational Pediatrics and Clinical Genetics, Ospedale Pediatrico Bambino Gesù, IRCCS, Rome, Italy

ARTICLE INFO

Keywords:
SLC52A2
RFVT2
Riboflavin
iPSC-derived motoneurons
Metabolic FLIM
FAD

ABSTRACT

Riboflavin transporter deficiency Type 2 (RTD2, OMIM #614707), formerly known as Brown-Vialetto-Van Laere Syndrome 2 (BVVLS 2), is a rare autosomal recessive neurodegenerative disorder caused by biallelic variants in the *SLC52A2* gene, encoding for riboflavin transporter 2 (RFVT2). This transporter plays a critical role in flavin cofactor delivery, particularly in the brain. Clinically, RTD2 presents with progressive hearing loss, optic atrophy, muscle weakness, respiratory issues, and pontobulbar palsy. Current treatment involves high-dose riboflavin and other supplements.

In this study we explored the molecular mechanisms behind RTD2, focusing on the dimerization of RFVT2 and the associated cellular stress mechanisms in patient-specific models. We demonstrated that RFVT2 exists as a homodimer and that pathogenic variants significantly impair its dimerization, which may contribute to the induction of ER stress. This hypothesis was supported by elevated levels of BiP, an ER stress marker, in patient iPSC-derived motor neurons. Similar findings were confirmed in patient-derived fibroblasts, where we also observed mitochondrial dysfunction and disrupted calcium signaling. Interestingly, no significant changes in FAD content were detected in both cell models, suggesting that proteotoxic stress may be a crucial pathogenic mechanism in RTD2, even in the absence of signs of FAD deficiency. FAD autofluorescence and FLIM measurements reinforce the occurrence of mitochondrial dysfunction in patient MNs.

These findings provide insight into the pathogenic mechanisms of RTD2, highlighting the critical role of RFVT2 misfolding, ER stress, and mitochondrial dysfunction in this neurodegenerative disorder.

Abbreviations: BVVL, Brown-Vialetto-Van Laere syndrome; ER, endoplasmic reticulum; FAD, flavin adenine dinucleotide; FLIM, fluorescence lifetime imaging microscopy; FMN, flavin mononucleotide; GPCA, Gaussia princeps protein complementation assay; iPSC, induced pluripotent stem cell; MNs, motor neurons; Rf, riboflavin; RFVT, riboflavin transporter; RTD2, riboflavin transporter deficiency Type 2; SOCE, store operated calcium entry; UPR, unfolded protein response.

* Corresponding author. Department of Biosciences, Biotechnologies, and Environment, University of Bari Aldo Moro, Via Orabona 4, 70125 Bari, Italy.
E-mail address: maria.barile@uniba.it (M. Barile).

[1] These authors contributed equally to this work.

https://doi.org/10.1016/j.abb.2025.110675
Received 16 May 2025; Received in revised form 14 October 2025; Accepted 21 November 2025
Available online 22 November 2025

1. Introduction

Riboflavin (Rf) transporter deficiency Type 2 (RTD2, OMIM #614707), formerly known as Brown Vialetto van Laere Syndrome 2 (BVVLS 2), is a rare autosomal recessive neurodegenerative disorder with a prevalence of less than 1 in 1.000.000. It is caused by biallelic pathogenic variations in the *SLC52A2* gene, which encodes for Rf transporter 2 (RFVT2). This carrier is ubiquitously expressed, but it is particularly relevant for the brain and, as recently demonstrated, for the blood-brain barrier in which its expression has been found to be age-dependent [1].

Clinically, RTD2 manifests with a range of debilitating symptoms, including hearing loss, muscle weakness (with predominant upper limb and axial weakness), respiratory compromise and pontobulbar palsy (commonly causing feeding and speech problems). Vision loss and sensory gait ataxia are also commonly noted in RTD2. Mental capabilities remain completely intact in all individuals. Current treatment involves high-dose Rf supplementation alongside antioxidants and other supplements, including coenzyme Q10, L-carnitine, vitamin C, vitamin E (Tocotrienols & Tocopherols), alpha lipoic acid, vitamin B-Complex, omega-3 fatty acids (EPA & DHA), and multivitamins (https://curertd.org/what-is-rtd/treatment/) [2].

The SLC52 family includes two other members, i.e., *SLC52A1* and *SLC52A3*, which encode for RFVT1 and RFVT3, respectively.

Furthermore, defects in these transporters are also linked to Rf-responsive diseases. The three plasma membrane transporters exhibit distinct tissue-specific expression profiles and functional and kinetic properties [3–5], which may explain the varying clinical manifestations associated with their defects.

RFVT2 is a 445-amino acid protein characterized by 11 transmembrane helices, connected by intra- and extra-cellular loops [6]. It mediates the transport of Rf, which, along with its derivatives, flavin adenine dinucleotide (FAD) and flavin mononucleotide (FMN), serves as crucial cofactor for numerous flavoenzymes, primarily located within mitochondria and peroxisomes, participating in the intermediary and terminal energy metabolism of fatty acids, carbohydrates, amino acids, pyridoxine, and choline [7].

A recently developed and reliable method for assessing the transport function of pathological variants of RFVT2 is the proteoliposome transport assay, allowing for individual testing of each mutant. This *in vitro* system has shown that all tested mutants exhibit an only marginally affected V_{max}, but significantly increased K_m; this finding could explain the responsiveness of patients to Rf therapy [4,8].

Investigations on RTD2 fibroblasts linked the effects of Rf transport loss with mitochondrial function. When grown in low extracellular Rf conditions, RTD2 patient fibroblasts showed a reduced Rf uptake [9] and a significant reduction in the intracellular levels of FMN and FAD together with impaired electron transport chain complex I and complex II activities [10].

Recent research has emphasized the simultaneous pathogenic role of cellular energy dysmetabolism and cytoskeletal disruption. In this regard, patient-specific RTD models created using induced pluripotent stem cell (iPSC) technology have revealed evidence of redox imbalance, which includes mitochondrial and peroxisomal dysfunction. This oxidative stress is likely responsible for cytoskeletal abnormalities, which are linked to the impaired differentiation of RTD motor neurons (MNs) [11].

Other studies performed on human-derived brain U87 cells demonstrated that, besides kinetic properties, pathogenic variants may affect stability/translational efficiency or alter the trafficking of the protein, thus resulting in retention of the protein in the endoplasmic reticulum (ER) [12]. Emerging evidence has also highlighted the role of ER stress in neurodegenerative diseases [13]. Singh et al. (2024) discuss how ER stress can activate the unfolded protein response (UPR), which, if unresolved, may lead to apoptosis and further neurodegeneration [14].

Dysregulation of Ca^{2+} signalling, in its various forms, is a key feature of neurodegeneration [15]. Recent studies have highlighted a direct link between ER stress and the so-called Store Operated Calcium Entry (SOCE) mechanism [16,17], which can also impact mitochondrial metabolism and dynamics [18].

Metabolic imaging of coenzymes involved in the cell metabolism, as FAD, can be performed by recording of autofluorescence decay functions in cultured cells using Fluorescence Lifetime Imaging Microscopy (FLIM) [19]. We investigated the behaviour of the known forms of FAD lifetime which, following binding to proteins, change from the unbound state, corresponding to the open conformation, to the bound/closed state [20–22] in RTD2 iPSC-derived motoneurons obtained from three RTD patients.

In this study we evaluated UPR^{ER} stress, disrupted calcium signalling and mitochondrial derangements in RTD2 patients by using both RTD2 iPSC-derived MNs from three compound heterozygote patients and fibroblasts from one patient. Searching for a potential source of these stresses, we also investigated the oligomeric state of the RFVT2 protein, demonstrating that recombinant RFVT2 exists as a dimer of about 100 kDa Mr, thus validating the homodimeric model of RFVT2 previously predicted by AlphaFold-Multimer [6].

2. Results

2.1. Dimerization of RFVT2 and its impairment in RTD variants

To gain further insight into the molecular effects of RFVT2 variants, we initially investigated RFVT2 dimerization by using recombinant 6His-tag protein purified by IMAC chromatography as described in Materials and Methods. Fig. 1A shows the results of a Sarkosyl-PAGE. The purified recombinant 6His-RFVT2 protein was run onto mildly denaturing Sarkosyl-gel and subsequently immunoblotted against the His-tag. The analysis revealed the presence of two cross-reactive bands: the first showed an apparent molecular mass of 45 kDa and the second, heavier band, of 100 kDa, virtually corresponding to the molecular masses of the monomeric and dimeric forms of RFVT2, respectively.

To further evaluate RFVT2 dimerization, we performed the *Gaussia princeps* protein complementation assay (GPCA) [23]. HEK293T cells were co-transfected with plasmids encoding for the Gluc1-RFVT2 and Gluc2-RFVT2 fusion proteins, generated as described in Materials and Methods. The expression levels of the two proteins in HEK293T cells are shown in Fig. 1B, left panel. We confirmed the RFVT2 dimerization with a normalized luminescence ratio (NLR) value of about 500 (Fig. 1B, right panel), as protein pairs are considered to be interactive if the NLR is above 3 [23]. In parallel we also tested RFVT2 in combination with the LAT1 transporter, which is known to form heterodimers with other proteins [24]. The GPCA analysis revealed an NLR value below the threshold for the Gluc1-LATS/GLUC2-RFVT2 combination, which further confirms the specificity of RFVT2 homodimerization. A control was made that the protein levels of Gluc1-LAT1 seem to be higher than those of Gluc1-RFVT2 in combination with Gluc2-RFVT2 (Fig. 1B, left panel).

The GPCA method was also used to assess whether patient-specific variants affect RFVT2 dimerization. We tested four pathological point variants resulting in the missense variant monomers S52F, L312P, G419S and R169C described in Refs. [25,26], in combination either with themselves (Gluc1/2-S52F, Gluc1/2-L312P, Gluc1/2-G419S, Gluc1/2-R169C) or with a different missense variant, according to the composition of dimers expected in affected compound heterozygote patients (Gluc1-S52F/Gluc2-L312P, Gluc1-S52F/Gluc2-L312P).

Each of the four Gluc1-RFVT2 point mutants either in combination with itself or with different Gluc2-RFVT2 mutants displayed expression levels in HEK293T cells ranging from 40 to 70 % of the protein levels observed when transfecting cells with Gluc1/2-WT (Fig. 2A). This suggests that the variations may destabilize the RFVT2 recombinant protein. Indeed, the W198* variant present in combination with R169C variant in a RTD2 patient was undetectable probably because of its

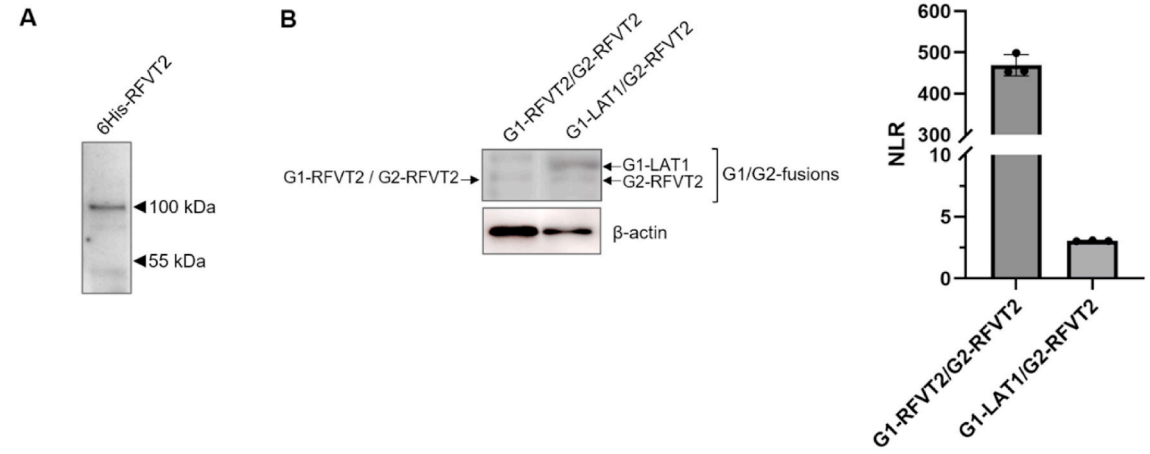

Fig. 1. Dimerization of RFVT2. (A) 0.28 μg of recombinant 6His-RFVT2 protein were solubilized in a buffer containing 50 mM Tris/Cl pH 6.8, 2.5 % Sarkosyl, 10 % glycerol, 35 mM DTE, 0.1 % bromophenol blue. The samples were separated by Sarkosyl-PAGE and immunoblotted with the anti-His peroxidase-conjugated antibody with a dilution of 1:40,000. (**B)** Pairwise combinations of Gluc1 (G1) and Gluc2 (G2) fusion constructs (i.e. Gluc1-RFVT2/LAT1 and Gluc2-RFVT2) were co-transfected in HEK293T cells. On the left, 10 % SDS-PAGE analysis of the protein levels of Gluc1-RFVT2/LAT1 and Gluc2-RFVT2 in HEK293T cells. Proteins were visualized by immunoblotting using a polyclonal anti-Gluc antibody, allowing for detection of both Gluc1 and Gluc2 fragments, albeit with lower efficiency for Gluc2. On the right, the interactions of Gluc1-RFVT2/LAT1 with Gluc2-RFVT2 proteins are reported. The luciferase activity was measured at 48 h post-transfection. NLR: normalized luminescence ratio, calculated as reported in the Materials and Methods section. Error bars represent standard deviations derived from three independent transfection experiments.

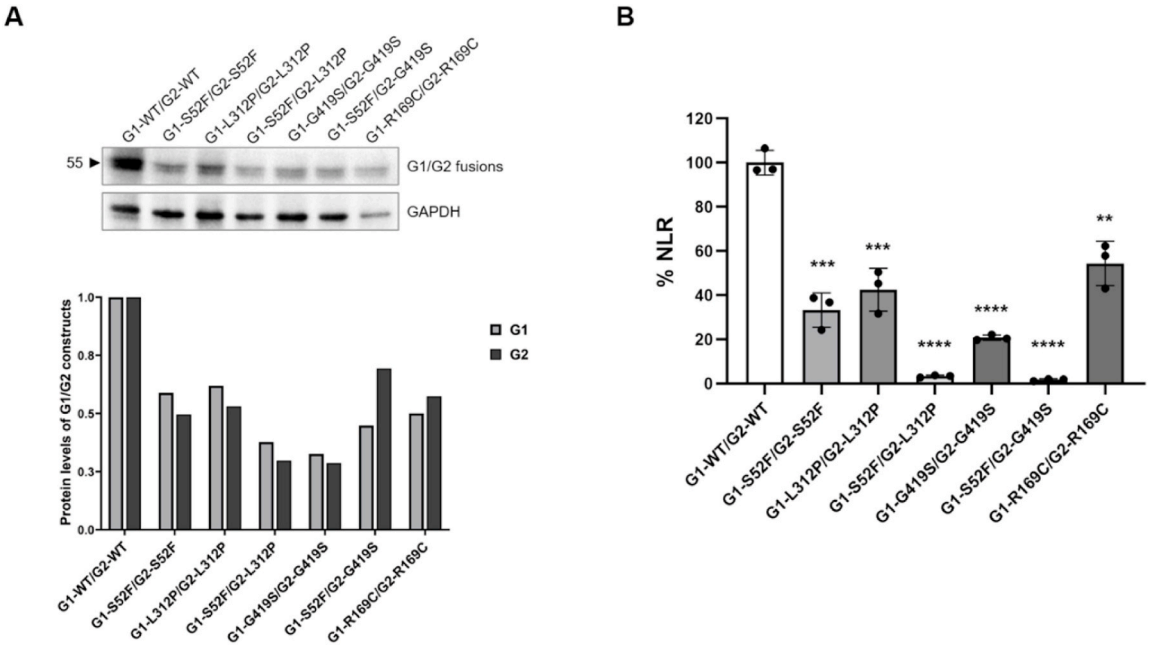

Fig. 2. Representative dataset for GPCA analysis of binary interactions between wt/mutant RFVT2 proteins. (A) Pairwise combinations of Gluc1-wt/mutant RFVT2 and Gluc2-wt/mutant RFVT2 fusion constructs were co-transfected in HEK293T cells. 10 % SDS-PAGE analysis of the protein levels of Gluc1-wt/mutant RFVT2 and Gluc2-wt/mutant RFVT2 proteins in HEK293T cells. Proteins were visualized by immunoblotting using a polyclonal anti-Gluc antibody. Quantification levels of the monomeric forms of RFVT2 WT and mutant proteins, each fused with Gluc1 or Gluc2, relative to that of GAPDH are represented as bar plots. **(B)** The interactions of Gluc1-wt/mutant RFVT2 and Gluc2-wt/mutant RFVT2 proteins are reported. Error bars represent standard deviations derived from three independent transfection experiments. Student's t-test: $^{**}p \leq 0.01$, $^{***}p \leq 0.001$, $^{****}p \leq 0.0001$.

degradation (data not shown), thus it has been excluded by the GPCA analysis.

The GPCA analyses revealed a decrease of the NLR value of 50 %–80 % for the mutant homodimers compared to the WT. An even stronger decrease (>90 %) was observed in heterodimers carrying two different variants, i.e., Gluc1-S52F/Gluc2-L312P or Gluc1-S52F/Gluc2-G419S (Fig. 2B).

2.2. UPR^{ER} in iPSC-derived MNs

We then speculated that the altered dimerization could cause ER stress, activating the integrated signalling pathway known as the UPR.

Therefore, we evaluated the protein content of the immunoglobulin heavy chain binding protein (BiP/Grp78), which is robustly induced in response to ER stress [27], in iPSC-derived MNs derived from three patients carrying the following *SLC52A2* pathogenic variants: c.155C >

T (p.S52F) and c.935T > C (p.L312P) (Patient 1, P1); c.505C > T (p.R169C) and c.1030_1031del (p.L344A*100) (Patient 2, P2); c.505C > T (p.R169C) and c.593G > A (p.W198*) (Patient 3, P3) and on healthy individual (Ctrl).

Whereas RFVT2 monomer levels appear to be similar in patient and control samples, an increase of BiP protein levels is observed for P1-3 (Fig. 3A). In particular P1, whose variants are associated with the lowest heterodimer formation (Fig. 2), displays a 15-fold increase compared to control. The BiP increase is accompanied by a decrease in α-tubulin levels in all patient samples (Fig. 3A), in agreement with previous results obtained with iPSCs [28]. The differential ER stress response across patients may reflect the specific RFVT2 variant combinations and their structural impact.

We also checked for possible mitochondrial UPR (UPR^{mt}) and we found just a slight increase (ranging from 1.6 to 2.4-fold) in the protein levels of the heat shock protein 60 (HSP60, a mitochondrial chaperonin) in all the patients tested when compared to the control (Fig. 3A).

To understand whether proteostasis derangement is correlated with scarcity of cellular/subcellular flavin delivery, we checked the protein levels of the mitochondrial flavoprotein SDHA (Fig. 3B), which typically correlate with FAD availability inside mitochondria, as well as its flavinylation level (FAD covalently bound per monomer of protein), assayed by on-gel UV fluorescence as described in Refs. [29,30] (Fig. 3B, lower panel).

Protein content appeared normal in patients' MNs compared to the control (or even slightly increased in patient P2). The degree of flavinylation follows the trend of apoprotein content, indicating that FAD levels are not limiting, thus, presumably, uncoupling the problem of flavin delivery in the cells to that of UPR activation.

2.3. Flavin content in iPSC-derived MNs

To gain further insight into flavin homeostasis in RTD patient-derived MNs, we measured Rf and flavin cofactors by HPLC in neutralized perchloric acid extracts of control and patient MN cell lysates [31]. Acid treatment allows the extraction of flavins that are either free or non-covalently bound to apoproteins [32].

Although an increase in FAD content—the most abundant flavin in these cells, accounting for approximately 80 % of the total acid-extractable flavin pool (Fig. S1A)—as well as in total flavin levels was observed in patient samples compared to controls, these differences did not reach statistical significance. Similarly, the levels of the less abundant flavins, FMN and Rf, remained unchanged (Table 1, Fig. S1B).

The lack of a significant decrease in flavin contents, observed in HPLC experiments, could derive from a compensatory mechanism due to either the presence of RFVT1 (Fig. 3A), or to the increased

Table 1
Cellular FAD, FMN, and Rf quantification (pmol/mg) in iPSC-derived MN samples.

	FAD	FMN	Rf	Total
C1	47.5 ± 9.3	5.6 ± 1.1	1.1 ± 0.3	54.1 ± 10.6
C2	48.5 ± 3.9	7.2 ± 2.0	2.5 ± 0.5	58.1 ± 5.4
P1	55.4 ± 1.3	7.1 ± 0.9	2.7 ± 0.3	65.2 ± 2.0
P2	51.8 ± 0.6	8.2 ± 0.4	2.1 ± 0.5	62.0 ± 1.4
P3	61.7 ± 5.9	7.0 ± 2.1	2.5 ± 0.7	71.2 ± 4.6

Data represent the mean ± SEM of at least two independent measurements. Statistical analysis was performed using Student's t-test: p > 0.05. See also Fig. S1B.

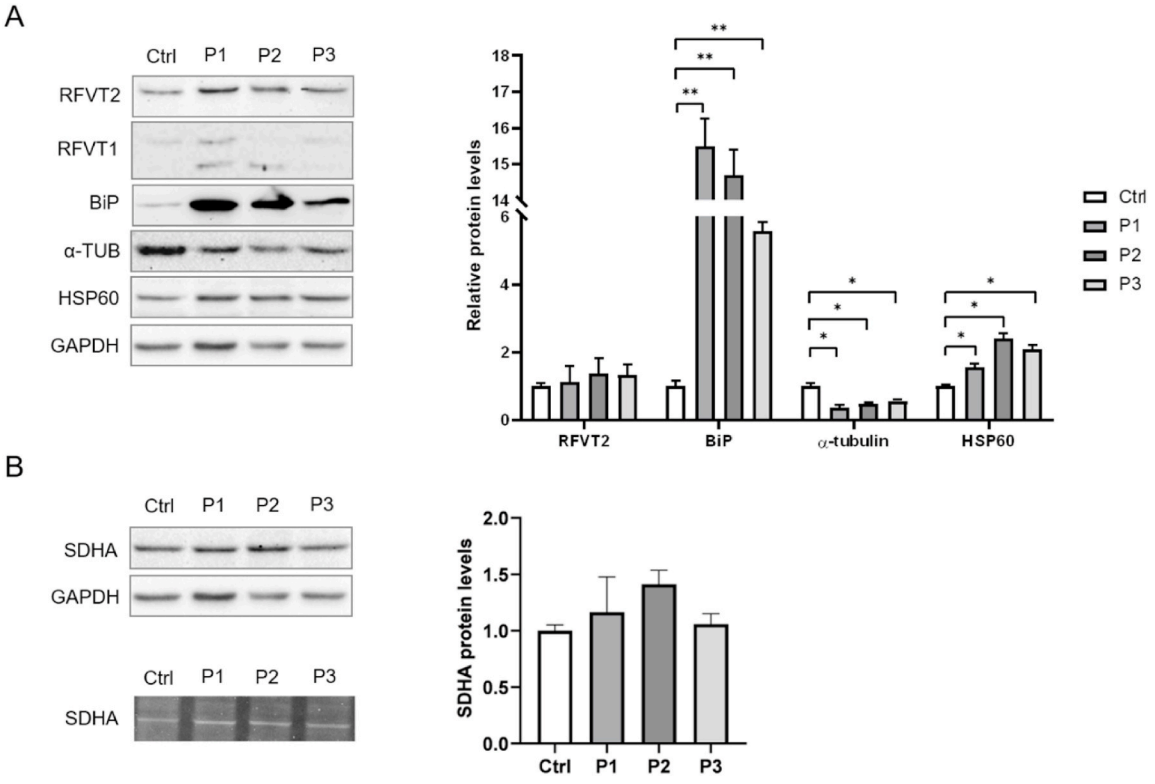

Fig. 3. Representative immunoblots for RFVT2, RFVT1, SDHA, BiP, HSP60 and α-tubulin. On the left, protein extracts (50 μg) from one control and three affected individuals' (P1-3) iPSC-derived MNs were separated by SDS-PAGE and immunoblotted with antibodies against RFVT2, RFVT1, BiP, α-Tubulin, HSP60 on the same membrane after stripping **(A)** and SDHA **(B, upper panel)**; GAPDH was used as loading control. **(B, lower panel)** Proteins from one control and three affected individuals' iPSC derived MNs (65 μg) were separated by SDS–PAGE. The flavin fluorescence of SDHA protein was visualized by UV irradiation of the unstained gel soaked in 10 % acetic acid.
On the right, protein intensities were normalized to that of GAPDH and reported as relative quantities with respect to the control (Ctrl). Error bars represent SEM of two independent experiments, student's t-test: *p < 0.05, **p < 0.01. RFVT1 was not quantify due to the low visibility of its bands.

transcriptional activity of SLC52A2 already observed in Ref. [25], whose mechanism is still not completely characterized.

Whatever the mechanism is, this piece of work confirms that the cellular phenotype described here and elsewhere [28] does not appear to be a direct consequence of an altered flavin supply.

2.4. Imbalance of the two FAD conformations in RTD MNs revealed by metabolic FLIM

To further explore the cellular status of flavins (mostly represented by FAD), we used FLIM, which allowed to reveal the free and bound states of FAD. This approach exploits FAD fluorescent properties exhibiting both long and short lifetimes, which are associated with the open and closed conformations, respectively. FAD lifetimes were determined in manually selected specific regions of interest (ROIs) corresponding to those cellular districts in which mitochondria were distributed. We performed FLIM experiments on Ctrl and RTD MNs, obtained after 30 days of differentiation (as described in Materials and Methods). Firstly, we carried out the confocal imaging and intensity analysis of the autofluorescence in MN samples and observed RTD MNs (Fig. 4A, Fig. S2) with higher green autofluorescence intensity with respect to Ctrl MNs. Subsequently, the FLIM microscopy carried out in the same fields of view highlighted that both the free/open and the bound/closed forms of the FAD molecule, were slightly increased in RTD MNs with respect to Ctrl MNs (Fig. 4B), considering the chromatic reference bar. The increase in free FAD lifetime values was observed in all patient-derived MNs, in particular for P1 MNs (Fig. 4C), whereas bound FAD lifetimes were significantly increased in all patients' MNs compared to Ctrl (Fig. 4D).

Interestingly, the amplitude of data population relating to the FAD open conformation (A1) was significantly increased in all patients' cells with respect to control mean value (Fig. 4E). In parallel the data population size of the closed conformation (A2) of FAD showed a significant increase in all patients' MNs (Fig. 4F), in agreement with the observed enhancement of autofluorescence intensity by confocal microscopy (Fig. 4A). Furthermore, the higher ratio of the A1/A2 fractions detected in patients' cells, particularly in P2 MNs suggested an unbalanced equilibrium between free and bound FAD molecules respect to control MNs (Fig. 4G).

2.5. Morphological characterization of P1 fibroblasts

In parallel with the experiments on iPSC-derived MNs, we introduced a non-neuronal cellular model, i.e. cell cultures of skin fibroblasts obtained from patient P1 (c.155C > T and c.935 T > C; p.S52F; p.L312P) and from age- and sex-matched controls (C1 and C2).

Patient-derived fibroblasts can be quickly established, easily maintained and can effectively recapitulate at least some of the key pathological hallmarks and dysfunctions observed in neurons [33].

First, bright-field micrographs of fibroblasts were taken to assess their morphological characteristics. No striking morphological differences were observed between low passages cultures of each cell line (Fig. 5). Nevertheless, P1 fibroblasts showed a decreased proliferation rate after reaching higher passages (>p15), suggesting a higher sensitivity to the stress resulting from successive passages and/or a tendency towards cellular senescence (data not shown).

2.6. RFVT2 and RFVT1 levels in P1 fibroblasts

Next, we evaluated RFVT2 and RFVT1 protein levels in P1 fibroblasts compared to that of controls. SDS-PAGE revealed the presence of a more abundant band cross-reacting with RFVT2 ab, that migrated at about 42 kDa, in good agreement with the theoretical molecular mass of this translocator (45.8 kDa) and a higher migrating band (51 KDa), presumably corresponding to a glycosylated form of the protein (not shown).

The quantitative analysis of the band did not reveal significant changes in the protein levels of neither RFVT2 monomer nor RFVT1 in P1 fibroblasts with respect to controls; whereas, differently from neuronal cell model, a normal α-tubulin content was found (Fig. 6).

2.7. Flavin content in P1 fibroblasts

We also analysed the flavin content in this cellular model by HPLC. While FMN and Rf levels (representing a small percentage of total flavin content) significantly decreased (50 and 80 %, respectively), FAD levels in P1 fibroblasts were consistent with control values (Table 2). This finding is in line with results obtained from the spectrophotometric enzymatic assay measuring Glutathione Reductase activation coefficient (GRAC), as previously described in human erythrocytes ([34] and references therein). This assay, which is based on the ability of externally added FAD to reactivate the apo-enzyme glutathione reductase present in cellular lysates in cases of hypovitaminosis, revealed a GRAC value of 1.1 for both controls and 1.2 for P1, indicating an acceptable FAD availability, according to Ref. [34].

2.8. UPR^{ER} in P1 fibroblasts

We further assessed the activation of UPR in P1 fibroblasts and found a 2-fold increase in the protein levels of BiP and HSP60 (Fig. 7A), suggesting a less pronounced UPR with respect to MN samples (Fig. 3A). Remarkably, a significant increase (about 1.7-fold) in transcript levels of BiP was revealed by RT-qPCR (Fig. 7B). We also checked the levels of the pro-apoptotic transcription factor C/EBP homologous protein (CHOP) and the XBox-Binding Protein 1 (xbp1), involved both in pro-survival or apoptotic pathways, depending on ER stress level [35]. We found a significant increase of transcript levels of both CHOP (about 1.5-fold) and xbp1 (about 2.5-fold) (Fig. 7B).

2.9. Mitochondrial derangements in P1 fibroblasts

Previous studies conducted on fibroblasts from a RTD patient, have revealed defects in the activities of complexes I and II of the respiratory chain when RTD2 patient' cells were grown in low extracellular Rf conditions [10]. Also, altered mitochondrial morphology, as assessed by electron microscopy, was proven by the same authors on a Drosophila model of RTD syndrome [10] and in RTD iPSC and iPSC derived-MNs [36,37].

Based on the same conceptual framework that explains the tight correlation between mitochondrial function and morphology [38], we analysed the mitochondrial network in living fibroblasts loaded with MitoTracker Green, a highly selective mitochondrial fluorophore.

Thanks to its insensitivity to changes in mitochondrial membrane potential, this dye can be used to label both healthy and unhealthy mitochondria. Additionally, it fluoresces only in the lipid environment of the mitochondria, so that very low concentrations produce a bright and stable stain against a negligible background (MitoTracker_Mitochondrion-Selective Probes - Thermo Fisher Scientific).

Epifluorescence assays showed highly fragmented mitochondria in patient's samples, where the classic "spaghetti" appearance, clearly visible in both the controls, was lost in most of the cells (Fig. 8A). The entity of mitochondria fragmentation was then quantitatively determined using Image J and calculating three parameters: form factor (FF), aspect ratio (AR), and mitochondria fragmentation count (MFC) (Fig. 8B). Form factor (FF, 4π·area/perimeter2) and aspect ratio (AR, ratio between major and minor axis) [39] are two dimensional descriptors whose values are proportional to mitochondrial branching/length and mitochondrial ellipticity, respectively [40]. Mitochondrial fragmentation count (MFC) was determined by counting discrete, non-contiguous mitochondrial elements and normalizing to the total pixel area of the mitochondrial network [41,42]. As shown in Fig. 8B, mitochondria in P1 fibroblasts appeared significantly more circular

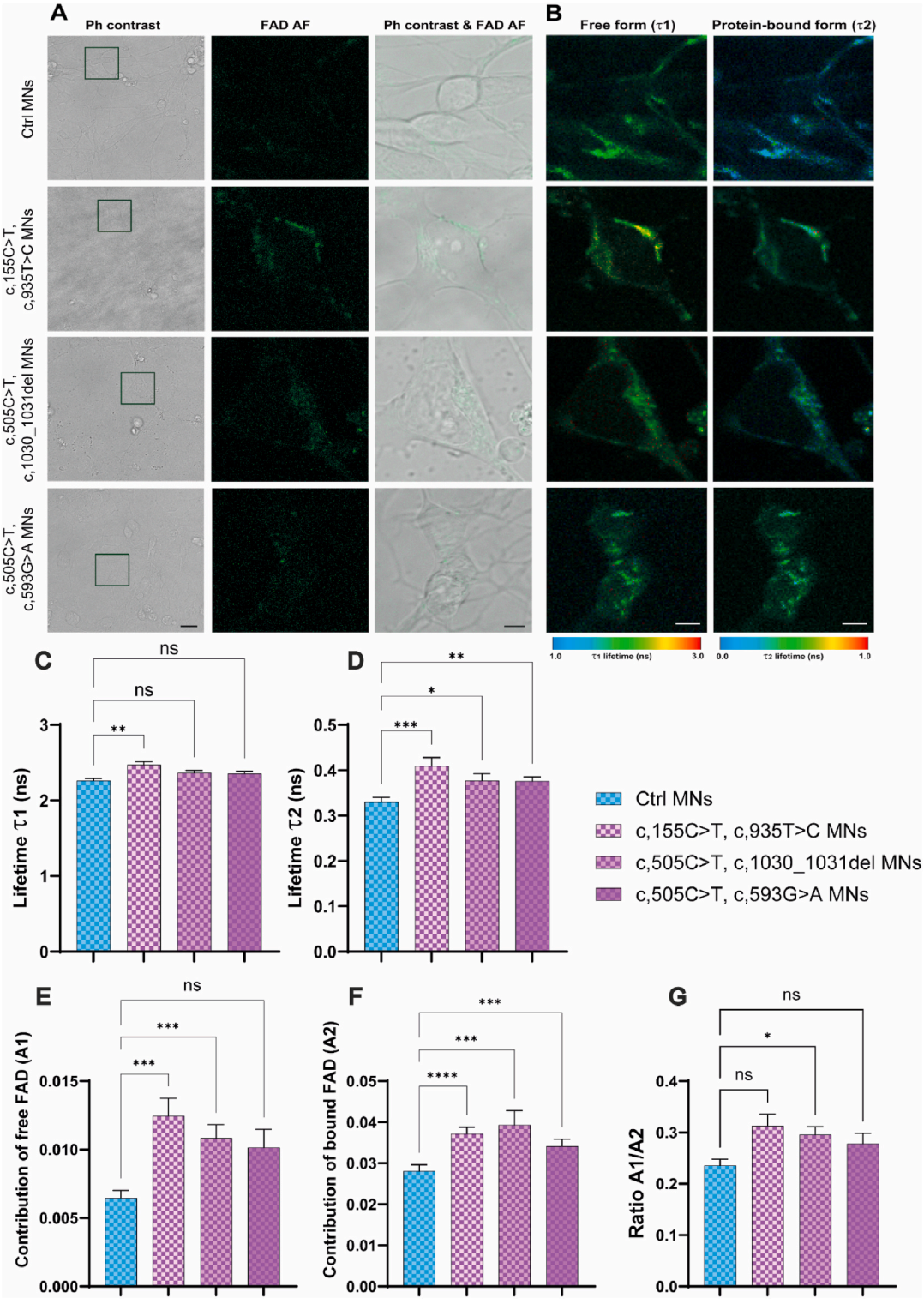

(caption on next page)

Fig. 4. Metabolic FLIM on RTD2 iPSC-derived motoneurons. (A) Confocal images of FAD autofluorescence in Ctrl and RTD MNs. The phase contrast shows the morphological features of Ctrl and RTD MNs (scale bar = 20 μm). The square indicates the area for which autofluorescence was analysed. The images represent FAD autofluorescence (FAD AF) acquired with Confocal mode. On the right, the images show the merge between phase contrast and autofluorescence (scale bar = 5 μm). **(B)** Corresponding FLIM analyses on Ctrl and RTD MNs. Images depict the spatial distribution of the lifetime values of free (τ1) and bound (τ2) FAD states. Different τ values were visualized *via* colour-coded lifetime scale bars (τ1: from 1.0 to 3.0 ns of range; τ2: from 0.0 to 1.0 ns of range). Scale bar = 5 μm. **C)** Bar graph quantification of the τ1 FAD lifetime values in Ctrl and RTD MNs. N of region of interest examined per sample = 89, 82, 59, 67 (Ctrl, P1, P2, P3) from 3 independent differentiation experiments. (**p < 0.01, Kruskal-Wallis with Dunnett's test; mean ± SEM) **(D)** Bar graph quantification of the τ2 FAD lifetimes in Ctrl and RTD MNs. N of region of interest examined per sample = 89, 82, 59, 67 (Ctrl, P1, P2, P3) from 3 independent differentiation experiments. (*p < 0.05, **p < 0.01, ***p < 0.001, Kruskal-Wallis with Dunnett's test; mean ± SEM) **(E)** Bar graph showing the contribution of free FAD (A1) fraction in Ctrl and RTD MNs. N of region of interest examined per sample = 89, 82, 59, 67 (Ctrl, P1, P2, P3) from 3 independent differentiation experiments. (***p < 0.001, Kruskal-Wallis with Dunnett's test; mean ± SEM) **(F)** Bar graph showing quantification of the contribution of bound FAD (A2). N of region of interest examined per sample = 89, 82, 59, 67 (Ctrl, P1, P2, P3) from 3 independent differentiation experiments. (***p < 0.001, ****p < 0.0001, Kruskal-Wallis with Dunnett's test; mean ± SEM). **(G)** Bar graph showing the ratio of A1/A2. N of region of interest examined per sample = 89, 82, 59, 67 (Ctrl, P1, P2, P3) from 3 independent differentiation experiments. (*p < 0.05, one-way ANOVA with Dunnett's test; mean ± SEM). (For interpretation of the references to colour in this figure legend, the reader is referred to the Web version of this article.)

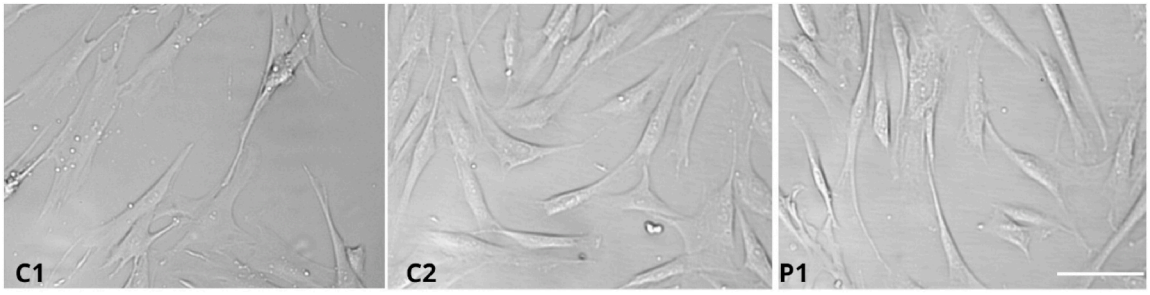

Fig. 5. Transmitted light micrographs of C1, C2 and P1 fibroblasts (scale bar 100 μm).

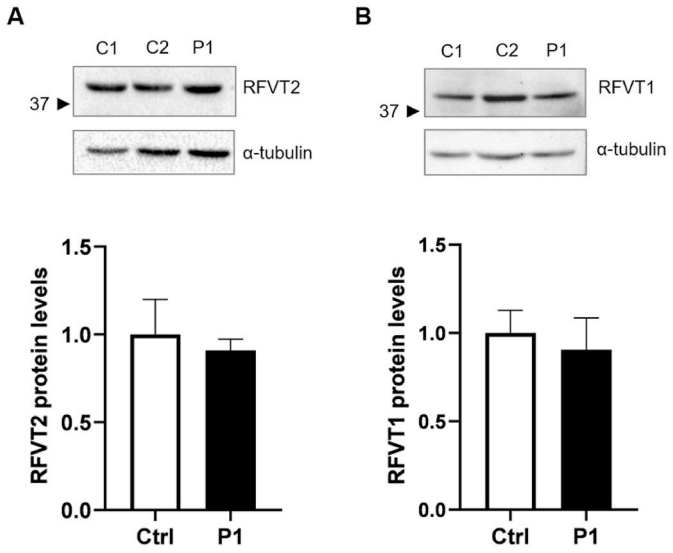

Fig. 6. Representative immunoblotting of RFVT2 and RFVT1 in P1 fibroblasts. Protein extracts (50 μg) from control (C1 and C2) and patient (P) fibroblasts were separated by SDS-PAGE and immunoblotted with polyclonal antibodies against RFVT2 **(A)** and RFVT1 **(B)** and a monoclonal antibody against α-tubulin, used as a loading control. RFVT2 and RFVT1 protein intensities were normalized to that of GAPDH and reported as relative quantities with respect to the mean of C1 and C2 individuals (Ctrl). Statistical analysis was performed using Student's t-test: p > 0.05.

(lower FF), exhibited reduced branching (lower AR), and showed increased fragmentation (higher MFC) compared to controls. Altogether, these parameters indicate a marked degree of mitochondrial fragmentation in patient cells compared to controls.

Interestingly, despite the normal FAD content as assessed in total cell extracts (Table 2), immunoblotting analyses revealed a significant decrease in SDHA protein content in P1 fibroblasts with respect to controls (Fig. 8C).

Table 2
Cellular FAD, FMN, and Rf quantification (pmol/mg) in fibroblast samples.

	FAD	FMN	Rf	Total
C1	98.1 ± 3.6	9.3 ± 1.1	2.0 ± 0.1	109.4 ± 2.7
C2	86.6 ± 1.5	7.7 ± 0.2	2.2 ± 0.2	96.5 ± 1.6
P1	101.6 ± 3.0	4.6 ± 0.1**	0.4 ± 0.1***	106.7 ± 2.9

Data represent the mean ± SEM of at least two independent measurements. Student's t-test: **p < 0.01, ***p < 0.001.

2.10. Cytosolic calcium dynamics in P1 fibroblasts

It is well established that changes in calcium concentration can benefit [43] or harm cells [44,45] depending on their specific subcellular localizations and kinetics.

In particular, a tight functional link between ER stress and calcium handling exists at the level of ER Ca^{2+} content, SOCE [46] and mitochondrial function and dynamics [47].

SOCE is initiated when low calcium levels in the ER, induced by calcium mediated agonists or SERCA pump inhibitors, activate STIM1, which then interacts with the Orai1 calcium channel on the plasma membrane, allowing calcium to enter the cell. The calcium influx is balanced by the SERCA pump, which restores calcium to the ER, maintaining cellular calcium homeostasis and enabling continuous SOCE [48].

Interestingly, SOCE has been recently demonstrated to be strictly related to ER stress and UPR signalling [16,17] (see discussion).

Thus, to assess the putative involvement of SOCE in the ER stress/UPR signaling measured in the BVVL patient, we performed live-cell calcium imaging experiments on Fura-2-loaded fibroblasts. Specifically, we applied a classical "Ca^{2+} re-addition" protocol (Fig. 9).

The ER Ca^{2+} store was depleted by a 10 min incubation with the SERCA inhibitor cyclopiazonic acid (CPA) in the absence of extracellular calcium, a maneuver that leads to a rapid loss of Ca^{2+} from the ER through constitutive release *via* the Ca^{2+}-leak channels. The amount of calcium released by the deposits, obtained by calculating the area under the curve registered in the first 10 min of CPA stimulation (AUC in

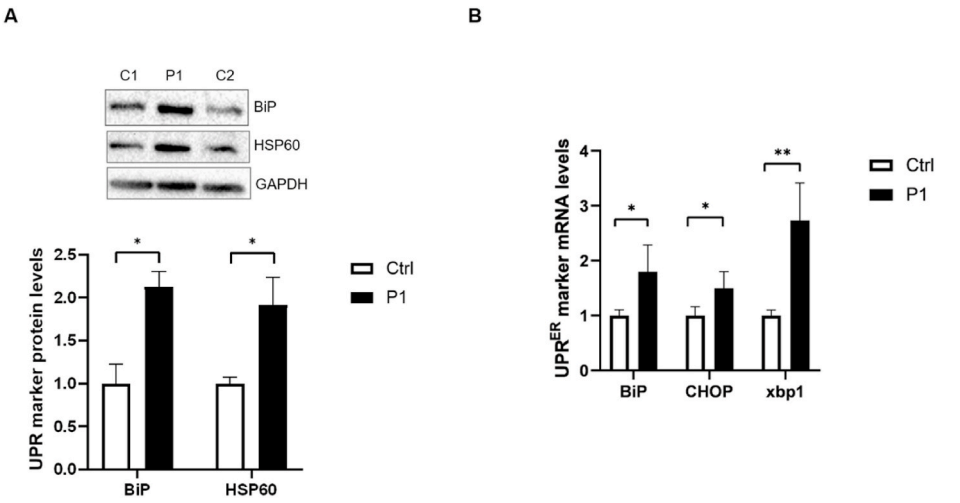

Fig. 7. Representative immunoblotting of BiP and HSP60 and qPCR analysis of UPR^{ER} markers in P1 and control fibroblasts. (A) Protein extracts (50 μg) from control (C1 and C2) and patient (P) fibroblasts were separated by SDS-PAGE and immunoblotted with a monoclonal antibody against BiP, a monoclonal antibody against HSP60 and a monoclonal antibody against GAPDH used as a loading control, on the same PVDF membrane after stripping. BiP and HSP60 protein intensities were normalized to that of GAPDH and reported as relative quantities with respect to the mean of C1 and C2 individuals (Ctrl). Error bars represent SEM of two independent experiments. Student's t-test: *p < 0.05. **(B)** RT-qPCR analysis of BiP, CHOP and Xbp-1 mRNA levels in P-fibroblasts compared to C1 and C2. Data were normalized to the housekeeping gene ACTB (β-actin) and reported as relative quantities with respect to the mean of C1 and C2 individuals (Ctrl). Error bars represent SD of three independent experiments. Student's t-test: *p < 0.05; **p < 0.01.

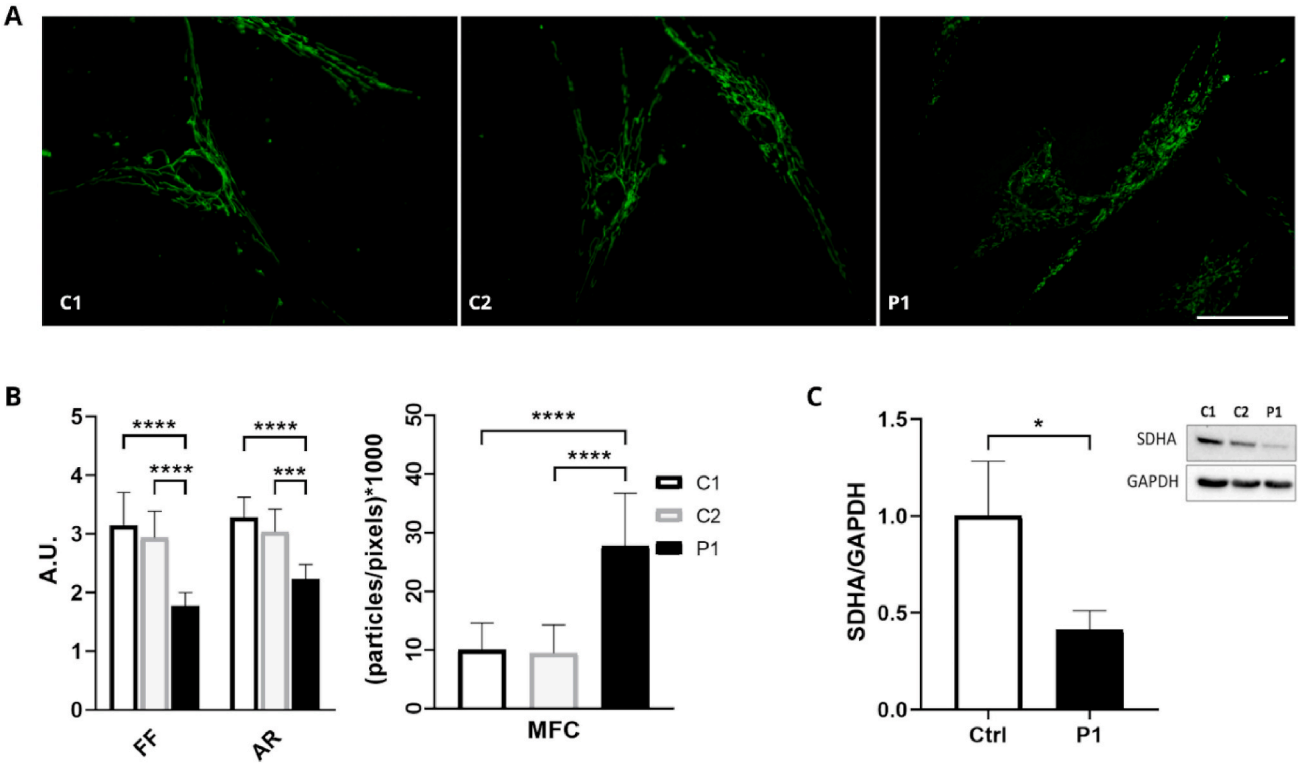

Fig. 8. Evidence of mitochondrial fragmentation in patient-derived fibroblasts (P1). (A) Representative epifluorescence micrographs of MitoTracker Green-stained mitochondria in C1, C2- and P1- live fibroblasts (scale bar 50 μm). **(B)** Histograms show the differences in aspect ratio (AR), form factor (FF), and mitochondrial fragmentation count (MFC) between control fibroblasts (C1 and C2) and patient-derived fibroblasts (P1). Means ± SD, ***p < 0.001, ****p < 0.0001. minimum of 15 cells. **(C)** Protein extracts (50 μg) from controls (C1 and C2) and patient's (P) fibroblasts were separated by SDS-PAGE and immunoblotted with a monoclonal antibody against SDHA and a monoclonal antibody against GAPDH, used as loading control, on the same PVDF membrane after stripping. SDHA protein intensities were normalized to that of GAPDH and reported as relative quantities with respect to the mean of C1 and C2 individuals (Ctrl). The error bars represent SEM of two independent experiments, student's t-test: *p < 0.05. (For interpretation of the references to colour in this figure legend, the reader is referred to the Web version of this article.)

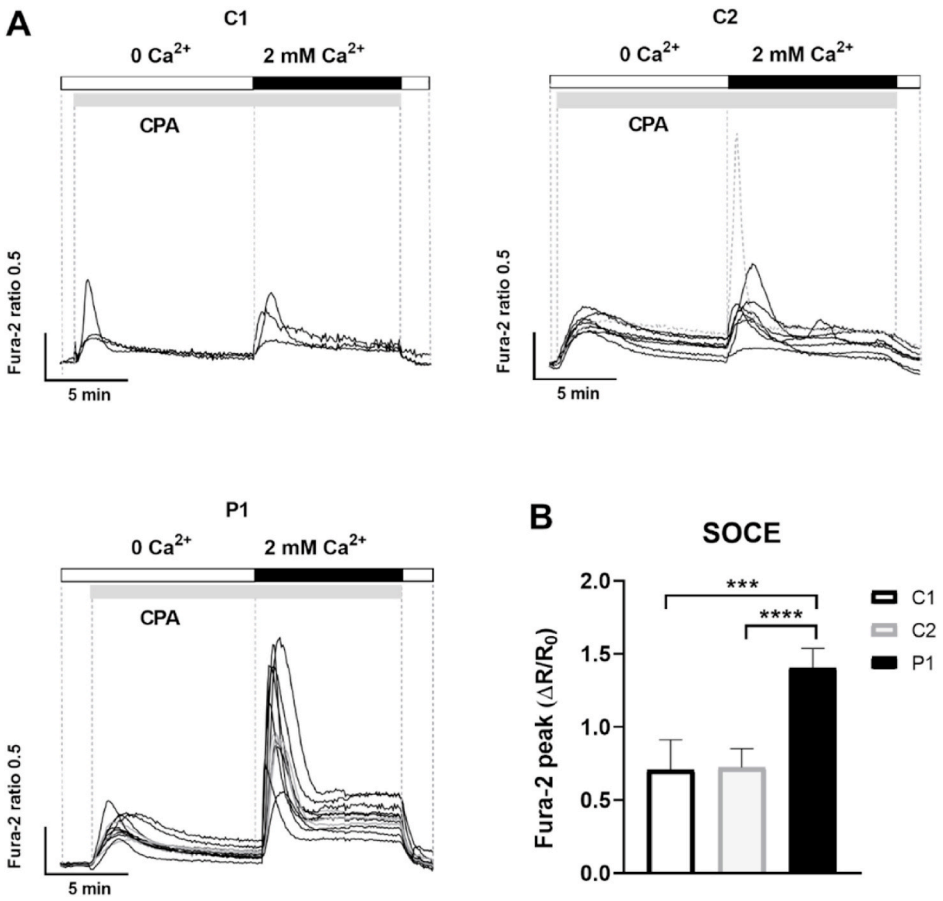

Fig. 9. Analysis of SOCE following cyclopiazonic acid stimulation of Fura-2 loaded fibroblasts. (A) Representative traces from C1, C2, and P1 fibroblasts are reported. Each trace shown was a Fura-2 ratio (340/380 nm) obtained for a single cell. **(B)** Histogram represents the SOCE (Fura-2 peak F340/380 after Ca^{2+} re-addition), means ± SEM of at least four independent experiments, student's t-test: ***$p < 0.001$; ****$p < 0.0001$.

Fig. 9A) represents an indirect measurement of their filling state. The rise in $[Ca^{2+}]_c$ induced by the re-addition of 2 mM $CaCl_2$ (Ca^{2+}) is indicative of SOCE.

Interestingly, while the amount of calcium released by the deposits was non-statistically different in all the samples, a significantly higher cytosolic peak after Ca^{2+}-readdiction (SOCE) was apparent in RTD patient's fibroblasts with respect to controls (Fig. 9B).

3. Discussion

Rf transporter deficiency Type 2 (RTD2) represents a significant clinical challenge, characterized by a spectrum of debilitating neurological symptoms while mostly maintaining intact cognitive functions. The pathophysiology of RTD2, driven by variations in the *SLC52A2* gene, reveals complex correlations between impaired Rf transport, mitochondrial dysfunction and cytoskeletal alteration [11]. Our findings enhance the understanding of the pathophysiology of RTD2, particularly regarding the oligomeric state of RFVT2 and its implications for cellular stress responses.

We definitively demonstrated RFVT2 dimerization both *in vitro* by Sarkosyl-PAGE with the recombinant RFVT2 and *in cellulo* by the advanced GPCA assay (Fig. 1). The two approaches concurred in demonstrating homodimerization of RFVT2. Our investigation also indicated that specific pathogenic variants result in impaired dimerization, as evidenced by reduced NLR in the GPCA assay (Fig. 2). Among the variants analysed, shown in the structure generated using UCSF Chimera (PDB 8XSM, [49]), the S52, which is substituted by a phenylalanine, is located within a transmembrane domain near the riboflavin binding pocket (Fig. S3); indeed, its mutation impairs the activity of the transporter [8]. Transmembrane α-helices also include the L312 and G419, which are substituted by a proline and a serine, respectively; the nature of this variations may destabilize local secondary structure (Fig. S3). On the contrary, the cysteine substitution of R169, located into an extracellular loop, may have less impact on the overall structure of the protein (Fig. S3).

The strongest impact on dimerization was observed when coupling monomers carrying two different variants corresponding to composed heterozygous patients (Fig. 2). This more pronounced effect may result from the combination of local destabilization of the two distinct regions of the protein affected by the amino acid substitutions.

The observed unchanged protein levels of RFVT2 monomer in patient samples (Fig. 3A) suggest that variants may trigger a compensatory mechanism performed by the cell transcriptional machinery, in line with previous findings showing an overall increase in RFVT2 mRNA levels of the same RTD2 patients analysed in the present study [25]. Since the variants, besides dimerization, also affect the transport activity [8], we propose that the normal cellular flavin levels assessed by HPLC (Table 1) is ensured by presence of the RFVT1 (Fig. 3A).

Our hypothesis is that the induction of ER stress related to RFVT2 variants, as evidenced by elevated BiP levels in patient derived-MNs (Fig. 3A), may also be due to the retention of RFVT2 in the ER, as has been reported for other mutants [12]. Altogether these findings are in favour of disruption of the proteostasis network caused by RFVT2 variants.

This proteostasis disruption could also explain the decrease of α-tubulin protein levels observed in RTD2 derived-MNs (Fig. 3A), in line with the work of Niceforo et al. [28], which shows alterations in cytoskeletal arrangements in iPSCs and MNs from RTD patients [28].

To gain further insight into the molecular mechanism underlying the ER stress response, we have used patient-derived fibroblasts, which are commonly exploited in biomedical research as a cost-effective disease model. Therefore, we have introduced here this model for a patient (P1) characterized by the highest levels of BiP. Indeed, we found a two fold increase of BiP protein levels in P1 fibroblasts (Fig. 7A), which is paralleled by the increase of HSP60, less evident on patient derived MNs (Fig. 3A). In addition, the demonstration that UPR response occurs in fibroblasts derives from the increase in mRNA levels of BiP, presumably due to the activation of ATF6 [27], even though we cannot exclude other signalling pathways connected to the increased transcript levels of xbp1 and CHOP (Fig. 7B). The increase of the last one might be part of an integrated stress response involving mitochondria [50]. Indeed, our data show that our P1 fibroblast model displays an apparent mitochondrial fragmentation (Fig. 8A), in line with literature linking RTD2 to mitochondrial structural abnormalities [26,36,37] and mitochondrial dynamics dysregulation in MNs [51].

Nevertheless, the cellular specific response to UPR deserves further investigation across different cellular models; for instance, in P1 fibroblasts α-tubulin content did not change with respect to that of controls (Fig. 6B), whereas the mitochondrial flavoprotein subunit SDHA is affected (Fig. 8C) differently from what occurs in patients MNs and in fibroblasts from another patient [9]. Consistently, defects of respiratory chain complex activity were not observed in patient derived MNs [51] but were demonstrated in fibroblasts from other patients [10].

Quite interestingly, HPLC analyses revealed normal or even increased levels of Rf and flavin cofactors in patients' derived-MNs (Table 1 and Fig. 4) that could be explained by the presence of RFVT1 (Fig. 3A) or by compensatory mechanisms leading to increased RFVT2 mRNA levels. Flavin homeostasis seems to be differently affected in P1 fibroblasts, in line with a cell-specific relative expression of RFVT1 and RFVT2 [52]. While the levels of the main cofactor FAD are normal, a significant reduction of about 50 and 80 % was found in its precursors (FMN and Rf) with respect to control (Table 2). These data also indicate that FAD availability alone does not guarantee a normal level of SDHA (Fig. 8C).

Quantitative analyses of the Metabolic FLIM markers highlighted different behaviour of the unbound and protein-bound FAD molecules between Ctrl and RTD MNs. The statistically significant augmented contribution of bound FAD (A2) in all patients derived motoneurons (Fig. 4F) is in line with the increased autofluorescence that may be explained by increased levels of oxidized species. This finding together with the altered ratio of the A1/A2 fractions detected in patients' cells (Fig. 4G) suggests an impaired mitochondrial functionality in RTD2 neuronal cells.

A further evidence of ER stress is given by the significantly increased SOCE in patient's fibroblasts, after ER emptying through the SERCA inhibitor cyclopiazonic acid (Fig. 9). There is, in fact, evidence that ER stress boosts SOCE [16] and that this action is mediated by a well known ER stress sensor, IRE1, which interacts with STIM1 to promote store-operated calcium entry [17].

We can speculate that in the fibroblast model, consisting of non-excitable cells endowed with a rather mild calcium influx, the increased SOCE may serve as compensatory mechanism to ER stress, allowing cells to restore protein folding and enhance mitochondrial metabolism. Quite predictably, if the compensatory response persists over time, it can lead to cellular dysfunction. In this context, the increased SOCE response could contribute to enhanced mitochondrial fragmentation (Fig. 8A and B) and malfunction (Fig. 8C). This aligns with the central hypothesis of this study, suggesting that dimerization defects of RFVT2 contribute to ER stress and UPR.

It is important to note that previous experiments [28] showed impaired calcium handling in RTD2 patient cells. Specifically, a reduced calcium peak upon ionomycin treatment was observed patients' derived MNs compared to controls [28,53]. In the present work, no significant difference in store content was observed between P1 and control fibroblasts.

A number of factors can account for these seemingly conflicting observations, including differences in the cell type examined, protocols and drugs used to induce store depletion. For example, ionomycin affects all the "non-acidic calcium stores" (ER, Golgi, mitochondria) [54], while cyclopiazonic acid specifically target ER. Additionally, cell-specific differences in calcium machinery can greatly influence results.

Despite some differences which are related to tissue-specificity, it is important to note that all studies on calcium signalling in RTD suggest that dysregulation of calcium homeostasis could contribute to the disease phenotype.

Future research must address the unanswered questions about the advantageous or disadvantageous role of the several subcellular calcium pathways in the various patient-derived cell models, especially in the cell types mostly impacted by the disease (such as MNs and cardiomyocytes).

Additionally, expanding the range of investigated variants will provide a more comprehensive understanding of how different variants impact RFVT2 functionality and patient phenotypes.

In summary, our findings underscore the complex nature of RTD2 pathophysiology, linking impaired RFVT2 dimerization defects to ER stress, calcium dysregulation and mitochondrial dysfunction. Further biochemical analyses aimed to clarify the impact of RFVT2 oligomerization on transport function as well as deep investigation of these pathways will be essential for developing effective therapeutic strategies and improving outcomes for affected individuals.

4. Materials and Methods

4.1. Purification of recombinant 6-his-RFVT2 and Sarkosyl-PAGE

The overexpression of the recombinant RFVT2 was obtained as previously described in Refs. [4,8]. Briefly, the *E. coli* codon-optimized cDNA coding for RFVT2 (GenScript) was cloned into the pH6EX3 plasmid. This construct was used to transform chemically competent *E. coli* Rosetta (Novagen) and protein expression was induced by adding 0.4 mM IPTG. After 4 h of incubation, cells were harvested by centrifugation. The bacterial pellet was suspended in a buffer containing 200 mM NaCl, 50 mM Hepes/Tris pH 7.5 and was subjected to mild sonication at 4 °C.

To purify RFVT2 in its active form, the lysate was centrifuged at 12,000×*g* for 10 min at 4 °C. The pellet was solubilized with 3 M urea, 0.8 % Sarkosyl, 200 mM NaCl, and 10 mM Tris/HCl pH 8.0 and centrifuged at 12,000×*g* for 10 min at 4 °C. The supernatant was applied onto a column containing the HIS-select nickel affinity gel (Merk P6611-25 ML). The column was then washed with a buffer containing 0.1 % C12E8, 200 mM NaCl, and 10 mM Tris/HCl pH 8.0. The recombinant protein was eluted by adding 50 mM imidazole to the same buffer [4,8].

For Sarkosyl-PAGE experiments, the purified RFVT2 was solubilized in a loading buffer containing 50 mM Tris/Cl pH 6.8, 2.5 % Sarkosyl, 10 % glycerol, 35 mM DTE, 0.1 % bromophenol blue. The electrophoresis was performed using a 10 % polyacrylamide gel under mild denaturing conditions. Indeed, differently from that described by Laemmli [55] Sarkosyl was used instead of SDS to prepare gel and running buffer. After Sarkosyl-PAGE, proteins were then blotted onto a nitrocellulose membrane, which was probed with the anti-His peroxidase-conjugated antibody (Merck A7058-1VL) with a dilution of 1:40,000.

4.2. Cell culture

The studies were conducted in compliance with the Code of Ethics of the World Medical Association (Declaration of Helsinki), and with national legislation and institutional guidelines (local institutional ethical committee, Ref. 1410_OPBG_2021, date of approval February 11, 2019). Informed consent was obtained from the subjects involved in the study.

The iPSC lines were obtained from patient skin fibroblasts following the nucleofection, as described in Ref. [56], using Epi5 Episomal iPSC Reprogramming Kit (A15960, Invitrogen) and the Nucleofection kit P2 solution (LOV4XP2024, Lonza) with 4D-Nucleofector System (Lonza). The pluripotency characterization is described in the following paper: for the patient carrying the variants c.155C > T (p.S52F) - c.935T > C (p.L312P) in Ref. [28] and for the patients carrying the variants c.505C > T (p.R169C) - c.1030_1031del (p.L344A*100) and the variants c.505C > T (p.R169C) and c.593G > A (p.W198*) in Ref. [25].

The generated iPSC lines carry the following SLC52A2 pathogenic variants: c.155C > T (p.S52F) and c.935T > C (p.L312P) (Patient 1, P1); c.505C > T (p.R169C) and c.1030_1031del (p.L344A*100) (Patient 2, P2); c.505C > T (p.R169C) and c.593G > A (p.W198*) (Patient 3, P3). Control iPSCs (Ctrl iPSCs) used in this study were derived from healthy individuals derived from Coriell (AG28851 and AG28869, Coriell Institute for Medical Research, USA) using non-integrating episomal technology.

- Maintenance of iPSCs

iPSCs were thawed in 6 well plates pre-coated with Geltrex (A1413202, Thermofisher) in DMEM-F12 (diluited 1:100, 31331-028, Gibco), and cultured in mTeSR1 Plus (05826, Stem Cell Technologies), supplemented with 10 μM Y-27632 (HY-10583, MedChem). The proliferating iPSCs were kept in mTeSR1 Plus medium, in the conditions of 37 °C, 5 % CO_2 and 5 % O_2. When they reached 60–70 % of confluence, they were split 1:3 (~4 x $10^{\wedge}5$ cells were grown in one well of the 6-well plates) with ethylenediaminetetraacetic acid (EDTA, E1644, Sigma Aldrich) and expanded with mTeSR1 Plus or frozen in mFreSR (05855, Stem Cell Technologies).

- Differentiation of iPSCs into motoneurons

iPSCs were differentiated into motoneurons (MNs) using an adapted protocol from Ref. [51]. When the iPSCs reached 30–40 % confluence, they were cultured into NeuroCult NS-A Basal Medium Human medium (05750, Stem Cell Technologies) for 10 days. At the 10th day, the medium was supplemented with 0.1 μM retinoic acid (R2625, Sigma Aldrich); from the 17th to the 25th days, it was supplemented with retinoic acid, 2 μM dorsomorphin (P5499, Sigma Aldrich) and 3 ng/mL activin A (120-14E, PeproTech). From the 25th to the 30th days, the NeuroCult NS-A Basal Medium Human medium was replaced with BrainPhys Neuronal Medium (05790, Stem Cell Technologies) and the following factors were added: NeuroCult SM1 Neuronal Supplement (SM1, 05711, Stem Cell Technologies), N-2 Supplement, 200 μM ascorbic acid (A4403, Sigma Aldrich), 20 ng/ml recombinant human glial-derived neurotrophic factor (GDNF, 450-10, PeproTech), 20 ng/ml Recombinant human brain-derived neurotrophic factor (BDNF, 450-02, PeproTech). During differentiation, the cells were split if they reached cultured at 70–80 % confluence and they were maintained 37 °C, 5 % CO_2 and 21 % O_2.

- Maintenance of fibroblasts

Dermal fibroblast cultures from one RTD patient (P1), and two healthy, age- and gender-matched controls C1 and C2 were incubated at 37 °C in a humidified atmosphere of 5 % (v/v) CO_2 in RPMI-1640 media (Lonza, BW12–167F) supplemented with 2 mmol/L of L-glutamine (Sigma Aldrich, St. Louis, MO, USA, G8540-25G), 10 % fetal bovine serum (Sigma Aldrich, St. Louis, MO, USA, F7524-500 ML), and 1 % penicillin/streptomycin (Sigma Aldrich, St. Louis, MO, USA, P4333-100 ML). For biochemical assays, cell cultures were transferred to 75 cm^2 culture flasks. Upon reaching sub-confluence, cells were washed in PBS and detached using 0.5 % Trypsin-EDTA solution (Sigma Aldrich, St. Louis, MO USA, T2610-100 ML). Cells were then resuspended in complete culture medium and then pelleted at 405×*g* (3 min) using a swinging arm centrifuge. The pellets were then washed twice in PBS (Sigma Aldrich, St. Louis, MO USA, D8537-500 ML) and re-pelleted. After the removal of PBS, fibroblasts pellets were snap-frozen using liquid nitrogen and stored at −80 °C.

For live-cell imaging experiments, cells were seeded on glass coverslips pretreated with 0.01 % poly-L-lisine (Sigma Aldrich, St. Louis, MO, USA, P2658-25 MG) at a cell density of $5X10^3$ cells/cm^2. After culturing for two days, controls and patient-derived coverslips (in duplicate) were subjected to mitochondria labelling using MitoTracker Green® (Thermofisher, Waltham, MA, USA, M7514) [57] or loaded with the cytosolic calcium sensor Fura 2-AM (Thermofisher, Waltham, MA, USA, F1221) for successive calcium imaging assays (see below). Cyclopiazonic Acid (CPA), a SERCA pump inhibitor, was purchased from Sigma-Aldrich (St. Louis, MO, USA; Cat. No. C1530).

4.3. Mitochondria fragmentation analysis

In order to highlight mitochondria, Mitogreen fluorescence micrographs were thresholded and converted into binary masks using mitochondria analyzer plugin for imageJ [58]. The entity of mitochondria fragmentation was then quantitatively determined using three descriptors: aspect ratio, form factor and mitochondria fragmentation count.

Aspect ratio (AR, ratio between major and minor axis) and form factor (FF, 4π·area/perimeter^2) [39] are two dimensional descriptors whose values are proportional respectively to mitochondrial ellipticity and mitochondrial branching and length [40]. Those parameters were calculated using Mitochondria Analyzer.

Mitochondria fragmentation count (MFC) was calculated by determining the area covered by the mitochondrial network and the total number of clearly identifiable discreet mitochondria following this equation: MFC=(n mitochondria/n pixel)*1000. A higher MFC value corresponds to a higher fragmentation of the mitochondrial network. The gathered values were analysed for normality using Shapiro-Wilk test. For normal distributed datasets (AR and FF), a *t*-test was performed to check for significant differences between the means. For non-normally distributed datasets (MFC), Kruskal-Wallis test was performed and post-hoc Dunn's test was conducted to highlight the statistical differences amongst the different groups. Statistical analysis was performed using GraphPad Prism8.

4.4. Immunoblotting analysis

Cell protein extracts were obtained by resuspending each cell pellet from the controls and patients in 100 μL lysis buffer containing 50 mmol/L Tris–HCl [pH 7.5], 1 % Triton X-100, 5 mmol/L β-mercaptoethanol [2-ME], 1 mmol/L NaF, 0.1 mmol/L PMSF, and 1 x protease inhibitor cocktail). The suspensions were passed through a 26G needle and incubated for 30 min on ice. After incubation, the cell suspensions were centrifuged at 13,000×*g* for 10 min at 4 °C, and the supernatants were collected as cell lysates.

Total cell protein extracts (50 μg) were dissolved in SDS/PAGE loading buffer (50 mM Tris-HCl, 2 % SDS, 10 % glycerol and 100 mM DTT, obtained from Sigma-Aldrich, St. Louis, MO, USA) and then separated on a 10 % T polyacrylamide gel, according to Laemmli [55]. Separated proteins were subsequently electro transferred onto a PVDF membrane (Amersham Biosciences, GE Healthcare, 10600023) using a transblot semidry electrophoretic transfer cell (Sigma-Aldrich, St. Louis, MO, USA). The membranes were probed with the following primary antibodies: succinate dehydrogenase complex flavoprotein subunit A (SDHA, Molecular probes, A-11142, 1:2000 dilution), RFVT2 (Thermo Fisher Scientific, Rockford, IL, USA, PA5-39700, 1:2000 dilution), RFVT1 (Thermo Fisher Scientific, Rockford, IL, USA, PA5-39703, 1:2000 dilution), HSP60 (Stressgen Biotechnologies, SPA-806, 1:1000 dilution), BiP (Cell signaling Technology, 3177, 1:1000 dilution), and α-tubulin (Sigma-Aldrich, St. Louis, MO, USA, T8203,1:5000 dilution) or GAPDH

(Cell signaling Technology, 21180, 1:5000 dilution) used as internal standard control. The bound antibodies were visualized using secondary anti-rabbit (Thermo Fisher Scientific, 31460) or anti-mouse (Thermo Fisher Scientific, 32430) IgG antibodies conjugated with peroxidase (1:2500 dilution). Protein detection was performed using ECL Western blotting detection reagents (Amersham, GE Healthcare, RPN2209), following the manufacturer's recommendations. Densitometry analysis was conducted using the Image Lab™ software (Bio-Rad) of Chem-iDoc™ (Bio-Rad) imaging system.

Immunoblotting experiments were also performed to check the efficacy of co-transfection for the GPCA experiments (see below). HEK-293T cells were grown and maintained in Dulbecco's modified Eagle's medium (DMEM), supplemented with 10 % FBS at 37 °C with 5 % CO_2 and then seeded in 6-well plates at a nominal confluence of $4.2x10^5$. After 18–24 h transfection mixes containing 1 μg of pSPICA-N2, 1 μg of pSPICA-N1 plasmids expressing test protein and 1 μg pUC51, plus JetPEI (Polyplus transfection, PEI MAX®, 24765-100) were added to the cells after 30′ of incubation. 2 h after transfection, cells were washed with 2 mL of PBS and lysed with 55 μl of Lysis buffer (Tris HCl pH 7.5 20 mM, NaCl 200 mM, EDTA 1 mM, NP-40 0.5 % and PIC). The samples were analysed on SDS/PAGE and detected by immunoblotting analysis with anti-Gluc (Thermo Fisher Scientific, PA1-181, 1:3000 dilution) incubated overnight in 5 % BSA under shaking at 4 °C and anti-β-actin (clone C4, MP Biomedicals, 1:20,000 dilution) incubated overnight in 5 % BSA under shaking at 4 °C, used as loading control, and revealed by chemiluminescence.

4.5. Quantification of cellular flavin content

Rf, FMN, and FAD were measured in neutralized perchloric acid extracts of cell lysates (0.2 mg) by HPLC as previously described [32, 59].

4.6. FLIM (fluorescence-lifetime imaging microscopy) measurements

Fluorescence lifetime imaging (FLIM) was carried out with a Leica TCS-SP8 FLIM (Leica Mycrosystems) confocal microscope, with time-correlated single photon counting (TCSPC) module PicoHarp 300 time-resolved unit (PicoQuant), with a pulsed White Light Laser (WLL) tunable in the range of 470–670 nm, 2 Internal SMD Spectral Detector Channels (PMT), through a HC PLAPO 63x/1.30 glycerol corr CS2 objective. FAD autofluorescence was excited at a wavelength of 470 nm and the emitted signal was detected in the 500–550 nm range. FLIM recordings were performed with a 40 MHz repetition rate, image size of 512x512 pixel, zoom factor 5x, and 200 repetitions. A minimum of 500 photons per pixels was collected for all FLIM acquisitions. For FLIM imaging experiments, $5 x 10^{\wedge 4}$ cells were grown in 35 mm optical plates (cod: 81156, Ibidi) previously coated with Geltrex (Thermofisher, A1413202). For each experiment, at least 10 individual cells were imaged, and all the experiments were repeated at least three times (n = 3). In each cell, FAD lifetimes were determined in manually selected specific regions of interest (ROIs) corresponding to those cellular districts in which mitochondria were distributed. A total number of 2–4 ROIs per cell were measured. Since the FAD fluorescence has both long and short lifetimes associated with free and protein-bound states, respectively, fitting results were obtained by applying a bi-exponential decay using the re-convolution fitting approach, and the quality of the fit was judged by the residual distribution and by the goodness of χ 2 value (close to 1). Unbound/open (long τ1) and bound/closed (short τ2) FAD forms' lifetimes were obtained from the SymPhoTime64 software (PicoQuant), together with the amplitude (A1 and A2) values of the data population relating to the 2 different lifetimes, and the autofluorescence intensity values within the area of each ROI. During the imaging of the experiments, the cells were maintained in HBSS medium to avoid interference with the red phenol present in the specific cell medium. Moreover, to ensure cell viability, it was used in a humidified environment at 37 °C and 5 % CO_2 in a microscope-compatible incubator system (Okolab).

4.7. Quantitative RT-PCR

Total cellular RNA was extracted from the cells using the RNeasy® Mini Kit (Qiagen, 74104) according to the manufacturer's protocol. The extracted RNA was then reverse-transcribed to cDNA using the RevertAid First Strand cDNA Synthesis Kit (Thermo Fisher Scientific, K1632) following the manufacturer's protocols. Quantitative real-time PCR analysis was performed using SYBR Green PCR Master Mix (Applied biosystems, 4309155) according to the manufacturer's instructions, with gene-specific primers listed in Table 3.

4.8. GPCA

A Gateway entry clone with codon-optimized ORF coding for WT RFVT2 was purchased from Addgene [60]. The variants (c.155C > T, c.935T > C, c.505C > T, c.1255G > A and c.593G > A resulting in p.S52F, L312P, R169C, G419S and W198*, respectively) were introduced using the Thermo Scientific Phusion Site-Directed Mutagenesis Kit (F-541). Due to codon-optimized nature of RFVT2 cDNA, the frameshift variant L344A*100 could not be mimicked. The resulting pEntry clones were transferred into the GPCA destination vectors pSPICA-N1 and pSPICA-N2. All constructs were verified by DNA sequencing.

HEK-293T cells were transfected using the reverse transfection method (JetPEI® (Polyplus transfection). Transfection mixes containing 100 ng of pSPICA-N2 and 100 ng of pSPICA-N1 plasmids expressing test proteins, plus JetPEI (Polyplus transfection), were dispensed in white 96-well plates. HEK-293T cells were then seeded on the DNA mixes at a concentration of $4.2 x 10^4$ cells per well.

At 48 h after transfection, cells were washed with 50 μL of PBS and lysed with 40 μL of Renilla lysis buffer (kit Renilla luciferase assay system, Promega, E2820) for 30 min with agitation. Gaussia princeps luciferase enzymatic activity was measured using a Berthold Centro LB960 luminometer by injecting 50 μL per well of luciferase substrate reagent (kit Renilla luciferase assay system, Promega) and counting luminescence for 10 s. Results are expressed as a fold change normalized over the sum of controls, specified herein as normalized luminescence ratio (NLR) [23]. For a given protein pair A/B, the NLR value corresponds to the ratio between the luminescence value of the two interacting proteins (Gluc1-A + Gluc2-B) and the sum of the luminescence values of each protein paired with the respective empty vector controls (Gluc1-A + Gluc2) and (Gluc1 + Gluc2-B).

$$NLR = (Gluc1\text{-}A + Gluc2\text{-}B)/[(Gluc1\text{-}A + Gluc2) + (Gluc1 + Gluc2\text{-}B)].$$

4.9. Cytosolic Ca^{2+} measurements with Fura-2 AM

For cytosolic Ca^{2+} recordings, the cells were seeded on 18 mm Ø glass coverslips and loaded with 3 μM Fura-2-AM (Thermo Fisher Scientific, Waltham, MA, USA) for 20 min at 37 °C, followed by 15 min in an extracellular solution to allow Fura-2 de-esterification. The coverslips with dye-loaded cells were mounted in an open perfusion chamber and recordings were carried out using an inverted Eclipse TE2000-S microscope (Nikon, Shinagawa, Tokyo, Japan) equipped for single cell fluorescence evaluations and imaging analysis. Each Fura-2-AM loaded sample was illuminated every 5s through a 40 × oil immersion objective (numerical aperture = 1.30) at 340 and 380 nm. The emitted fluorescence was passed through a dichroic mirror, filtered at 510 nm (Omega Optical, Brattleboro, VT, USA), and captured by a cooled CCD CoolSNAP HQ camera (Photometrics, Tucson, AZ, USA). Fluorescence measurements were carried out using the MetaFluor Fluorescence Ratio Imaging Software (Version 7.7.3.0, Molecular Devices, San Jose, CA, USA) [61]. Responses to the various stimuli were expressed as the change in fluorescence normalized to the basal fluorescence ratio observed in the

Table 3
Oligonucleotide primer sequences.

Gene	Forward primer	Reverse primer
B-Actin	5′-CTGGGAGTGGGTGGAGGC-3′	5′-TCAACTGGTCTCAAGTCAGTG-3′
BiP	5′-CGGGCAAAGATGTCAGGAAAG-3′	5′-TTCTGGACGGGCTTCATAGTAGAC-3′
CHOP	5′-ACCAAGGGAGAACCAGGAAACG-3′	5′-TCACCATTCGGTCAATCAGAGC-3′
xbp-1	5′-TTACGAGAGAAAACTCATGGC-3′	5′-GGGTCCAAGTTGTCCAGAATGC-3′

absence of stimuli ($\Delta R/R_0$).

4.10. Data analysis and statistics

The data obtained were represented using mean ± SEM or SD. For all experiments, multiple technical replicates and biological replicates were utilized and a minimum of two independent experiments were performed for each assay. GraphPad-Prism software (Prism 8) was used to analyze the data.

For FLIM experiments quantification and statistical analyses of the control cells were reported as the mean of the data derived from the two cell lines (AG28851 and AG28869). Significance was tested using ANOVA test.

For Cytosolic Ca^{2+} Measurements with Fura-2 AM, the results were tested for normality using Shapiro-Wilk test, and difference of the means were assessed using Student's t-test or Mann-Whitney ranks test.

In all the other experiments, Student's t-test was used.

4.11. Other assays

Protein concentration was determined according to Bradford [62], using bovine serum albumin as a standard and the Bio-Rad protein assay dye reagent concentrate (Bio-Rad).

UV-fluorescence analysis for evaluating flavinylation levels of SDHA was performed on control and RTD2 iPSC-derived MNs total cell lysates (65 μg) essentially as in Ref. [63].

CRediT authorship contribution statement

Maria Tolomeo: Writing – review & editing, Writing – original draft, Investigation, Formal analysis, Conceptualization. **Valentina Magliocca:** Writing – original draft, Methodology, Investigation, Formal analysis, Conceptualization. **Stefania Petrini:** Writing – original draft, Methodology, Investigation, Formal analysis. **Alessia Nisco:** Investigation, Formal analysis, Conceptualization. **Roberto Barbaro:** Investigation, Formal analysis. **Martina Lanza:** Investigation, Formal analysis. **Michela Piccione:** Investigation, Formal analysis. **Anna Maria Giudetti:** Writing – review & editing, Methodology. **Keith Massey:** Writing – review & editing. **Lara Console:** Methodology, Investigation, Formal analysis. **Cesare Indiveri:** Writing – review & editing. **Katia Zanier:** Writing – review & editing, Methodology. **Enrico Bertini:** Supervision, Funding acquisition. **Tiziana Persichini:** Supervision, Funding acquisition. **Claudia Compagnucci:** Writing – original draft, Supervision, Funding acquisition. **Matilde Colella:** Writing – original draft, Supervision. **Maria Barile:** Writing – review & editing, Writing – original draft, Supervision, Funding acquisition, Conceptualization.

Funding sources

This work was supported by a grant from Cure RTD Foundation (Year 2023) to MB. This work was also supported by the Italian Ministry of Health with Current Research funds, RCR-2022-23682289 and SG-2021-12373714; from MNESYS (to CC and EB), the Cure RTD Foundation, Cure RTD Italia Odv, Fondazione Bambino Gesù.

Conflict of interest

The authors declare that they have no known competing financial interests or personal relationships that could have appeared to influence the work reported in this paper.

Appendix A. Supplementary data

Supplementary data to this article can be found online at https://doi.org/10.1016/j.abb.2025.110675.

Data availability

Data will be made available on request.

References

[1] S.W. Yee, J. Wang, K.M. Giacomini, Rare diseases linked to mutations in vitamin transporters expressed in the human blood-brain barrier, Clin. Pharmacol. Ther. 116 (2024) 1513–1520.
[2] E. Bertini, C. Compagnucci, K. Massey, Riboflavin transporter deficiency or brown-vialetto-van laere syndrome, Reference Module in, Neuroscience and Biobehavioral Psychology 4 (2025) 13–20.
[3] M. Barile, T.A. Giancaspero, P. Leone, M. Galluccio, C. Indiveri, Riboflavin transport and metabolism in humans, J. Inherit. Metab. Dis. 39 (2016) 545–557.
[4] L. Console, M. Tolomeo, M. Colella, M. Barile, C. Indiveri, Reconstitution in proteoliposomes of the recombinant human riboflavin transporter 2 (SLC52A2) overexpressed in E. coli, Int. J. Mol. Sci. 20 (2019).
[5] L. Console, M. Tolomeo, L. Travo, D. Giudice, A. Nisco, M. Barile, C. Indiveri, Production of the recombinant human riboflavin transporters SLC52A1, 3 and functional assay in proteoliposomes, Arch. Biochem. Biophys. (2025) 110327.
[6] O. Ben Mariem, S. Saporiti, U. Guerrini, T. Laurenzi, L. Palazzolo, C. Indiveri, M. Barile, E. De Fabiani, I. Eberini, In silico investigation on structure-function relationship of members belonging to the human SLC52 transporter family, Proteins 91 (2023) 619–633.
[7] M. Tolomeo, A. Nisco, P. Leone, M. Barile, Development of novel experimental models to study flavoproteome alterations in human neuromuscular diseases: the effect of Rf therapy, Int. J. Mol. Sci. 21 (2020).
[8] L. Console, M. Tolomeo, J. Cosco, K. Massey, M. Barile, C. Indiveri, Impact of natural mutations on the riboflavin transporter 2 and their relevance to human riboflavin transporter deficiency 2, IUBMB Life 74 (2021) 618–628.
[9] M. Ciccolella, S. Corti, M. Catteruccia, S. Petrini, G. Tozzi, T. Rizza, R. Carrozzo, M. Nizzardo, A. Bordoni, D. Ronchi, A. D'Amico, C. Rizzo, G.P. Comi, E. Bertini, Riboflavin transporter 3 involvement in infantile brown-vialetto-van laere disease: two novel mutations, J. Med. Genet. 50 (2013) 104–107.
[10] A. Manole, Z. Jaunmuktane, I. Hargreaves, M.H.R. Ludtmann, V. Salpietro, O. D. Bello, S. Pope, A. Pandraud, A. Horga, R.S. Scalco, A. Li, B. Ashokkumar, C. M. Lourenco, S. Heales, R. Horvath, P.F. Chinnery, C. Toro, A.B. Singleton, T. S. Jacques, A.Y. Abramov, F. Muntoni, M.G. Hanna, M.M. Reilly, T. Revesz, D. M. Kullmann, J.E.C. Jepson, H. Houlden, Clinical, pathological and functional characterization of riboflavin-responsive neuropathy, Brain : J. Neurol. 140 (2017) 2820–2837.
[11] F. Colasuonno, C. Marioli, M. Tartaglia, E. Bertini, C. Compagnucci, S. Moreno, New insights into the neurodegeneration mechanisms underlying riboflavin transporter deficiency (RTD): involvement of energy dysmetabolism and cytoskeletal derangement, Biomedicines 10 (2022).
[12] V.S. Subramanian, R. Kapadia, A. Ghosal, H.M. Said, Identification of residues/sequences in the Human Riboflavin transporter-2 that is Important for Function and Cell Biology, *Nutrition & Metabolism*, vol. 12, 2015, p. 13.
[13] C. Hetz, S. Saxena, ER stress and the unfolded protein response in neurodegeneration, Nat. Rev. Neurol. 13 (2017) 477–491.
[14] R. Singh, N. Kaur, V. Choubey, N. Dhingra, T. Kaur, Endoplasmic reticulum stress and its role in various neurodegenerative diseases, Brain Res. 1826 (2024) 148742.
[15] E. Pchitskaya, E. Popugaeva, I. Bezprozvanny, Calcium signaling and molecular mechanisms underlying neurodegenerative diseases, Cell Calcium 70 (2018) 87–94.
[16] I.X. Zhang, J. Ren, S. Vadrevu, M. Raghavan, L.S. Satin, ER stress increases store-operated Ca(2+) entry (SOCE) and augments basal insulin secretion in pancreatic beta cells, J. Biol. Chem. 295 (2020) 5685–5700.

[17] A. Carreras-Sureda, X. Zhang, L. Laubry, J. Brunetti, S. Koenig, X. Wang, C. Castelbou, C. Hetz, Y. Liu, M. Frieden, N. Demaurex, The ER stress sensor IRE1 interacts with STIM1 to promote store-operated calcium entry, T cell activation, and muscular differentiation, Cell Rep. 42 (2023) 113540.
[18] J. Nan, J. Li, Y. Lin, M. Saif Ur Rahman, Z. Li, L. Zhu, The interplay between mitochondria and store-operated Ca(2+) entry: emerging insights into cardiac diseases, J. Cell Mol. Med. 25 (2021) 9496–9512.
[19] A.A. Heikal, Intracellular coenzymes as natural biomarkers for metabolic activities and mitochondrial anomalies, Biomarkers Med. 4 (2010) 241–263.
[20] O.I. Kolenc, K.P. Quinn, Evaluating cell metabolism through autofluorescence imaging of NAD(P)H and FAD, Antioxidants Redox Signal. 30 (2019) 875–889.
[21] M.S. Islam, M. Honma, T. Nakabayashi, M. Kinjo, N. Ohta, pH dependence of the fluorescence lifetime of FAD in solution and in cells, Int. J. Mol. Sci. 14 (2013) 1952–1963.
[22] P.A.W. van den Berg, K.A. Feenstra, A.E. Mark, H.J.C. Berendsen, A.J.W.G. Visser, Dynamic conformations of Flavin Adenine dinucleotide: simulated molecular dynamics of the Flavin cofactor related to the time-resolved fluorescence characteristics, J. Phys. Chem. B 106 (2002) 8858–8869.
[23] P. Cassonnet, C. Rolloy, G. Neveu, P.O. Vidalain, T. Chantier, J. Pellet, L. Jones, M. Muller, C. Demeret, G. Gaud, F. Vuillier, V. Lotteau, F. Tangy, M. Favre, Y. Jacob, Benchmarking a luciferase complementation assay for detecting protein complexes, Nat. Methods 8 (2011) 990–992.
[24] L. Napolitano, M. Galluccio, M. Scalise, C. Parravicini, L. Palazzolo, I. Eberini, C. Indiveri, Novel insights into the transport mechanism of the human amino acid transporter LAT1 (SLC7A5). Probing critical residues for substrate translocation, Biochim. Biophys. Acta Gen. Subj. 1861 (2017) 727–736.
[25] V. Magliocca, A. Lanciotti, E. Ambrosini, L. Travaglini, V. D'Ezio, V. D'Oria, S. Petrini, M. Catteruccia, K. Massey, M. Tartaglia, E. Bertini, T. Persichini, C. Compagnucci, Modeling riboflavin transporter deficiency type 2: from iPSC-derived motoneurons to iPSC-derived astrocytes, Front. Cell. Neurosci. 18 (2024) 1440555.
[26] C. Marioli, M. Muzzi, F. Colasuonno, C. Fiorucci, N. Cicolani, S. Petrini, E. Bertini, M. Tartaglia, C. Compagnucci, S. Moreno, Caspase-dependent apoptosis in Riboflavin Transporter Deficiency iPSCs and derived motor neurons, Cell Death Discov. 10 (2024) 54.
[27] N. Hiramatsu, V.T. Joseph, J.H. Lin, Monitoring and manipulating mammalian unfolded protein response, Methods Enzymol. 491 (2011) 183–198.
[28] A. Niceforo, C. Marioli, F. Colasuonno, S. Petrini, K. Massey, M. Tartaglia, E. Bertini, S. Moreno, C. Compagnucci, Altered cytoskeletal arrangement in induced pluripotent stem cells (iPSCs) and motor neurons from patients with riboflavin transporter deficiency, in: Disease Models & Mechanisms, vol. 14, 2021.
[29] C. Brizio, R. Brandsch, D. Bufano, L. Pochini, C. Indiveri, M. Barile, Over-expression in Escherichia coli, functional characterization and refolding of rat dimethylglycine dehydrogenase, Protein Expr. Purif. 37 (2004) 434–442.
[30] T.A. Giancaspero, R. Wait, E. Boles, M. Barile, Succinate dehydrogenase flavoprotein subunit expression in Saccharomyces cerevisiae–involvement of the mitochondrial FAD transporter, Flx1p, FEBS J. 275 (2008) 1103–1117.
[31] M. Tolomeo, G. Chimienti, M. Lanza, R. Barbaro, A. Nisco, T. Latronico, P. Leone, G. Petrosillo, G.M. Liuzzi, B. Ryder, M. Inbar-Feigenberg, M. Colella, A.M.S. Lezza, R.K.J. Olsen, M. Barile, Retrograde response to mitochondrial dysfunctions associated to LOF variations in FLAD1 exon 2: unraveling the importance of RFVT2, Free Radic. Res. 56 (2022) 511–525.
[32] P. Leone, M. Tolomeo, M. Barile, Continuous and discontinuous approaches to Study FAD synthesis and degradation catalyzed by purified recombinant FAD synthase or cellular fractions, Methods Mol. Biol. 2280 (2021) 87–116.
[33] D. Hoffmann, A. Haapasalo, Patient-derived skin fibroblasts as a model to study frontotemporal lobar degeneration, Neural Regen. Res. 17 (2022) 2669–2671.
[34] A. Tummolo, P. Leone, M. Tolomeo, R. Solito, M. Mattiuzzo, F.R. Lepri, T. Lore, R. Cardinali, D. De Giovanni, S. Simonetti, M. Barile, Combined isobutyryl-CoA and multiple acyl-CoA dehydrogenase deficiency in a boy with altered riboflavin homeostasis, JIMD reports 63 (2022) 276–291.
[35] A.H. Lee, N.N. Iwakoshi, L.H. Glimcher, XBP-1 regulates a subset of endoplasmic reticulum resident chaperone genes in the unfolded protein response, Mol. Cell Biol. 23 (2003) 7448–7459.
[36] F. Colasuonno, A. Niceforo, C. Marioli, A. Fracassi, F. Stregapede, K. Massey, M. Tartaglia, E. Bertini, C. Compagnucci, S. Moreno, Mitochondrial and peroxisomal alterations contribute to energy dysmetabolism in Riboflavin transporter deficiency, Oxid. Med. Cell. Longev. 2020 (2020) 6821247.
[37] F. Colasuonno, E. Bertini, M. Tartaglia, C. Compagnucci, S. Moreno, Mitochondrial abnormalities in induced pluripotent stem cells-derived motor neurons from patients with Riboflavin transporter deficiency, Antioxidants 9 (2020).
[38] M. Giacomello, A. Pyakurel, C. Glytsou, L. Scorrano, The cell biology of mitochondrial membrane dynamics, Nat. Rev. Mol. Cell Biol. 21 (2020) 204–224.
[39] W.J. Koopman, S. Verkaart, H.J. Visch, F.H. van der Westhuizen, M.P. Murphy, L. W. van den Heuvel, J.A. Smeitink, P.H. Willems, Inhibition of complex I of the electron transport chain causes O2-. -mediated mitochondrial outgrowth, Am. J. Physiol. Cell Physiol. 288 (2005) C1440–C1450.
[40] K. Trudeau, A.J. Molina, S. Roy, High glucose induces mitochondrial morphology and metabolic changes in retinal pericytes, Investig. Ophthalmol. Vis. Sci. 52 (2011) 8657–8664.
[41] J. Rehman, H.J. Zhang, P.T. Toth, Y. Zhang, G. Marsboom, Z. Hong, R. Salgia, A. N. Husain, C. Wietholt, S.L. Archer, Inhibition of mitochondrial fission prevents cell cycle progression in lung cancer, in: FASEB Journal vol. 26, official publication of the Federation of American Societies for Experimental Biology, 2012, pp. 2175–2186.
[42] M.J. Durand, K. Ait-Aissa, V. Levchenko, A. Staruschenko, D.D. Gutterman, A. M. Beyer, Visualization and quantification of mitochondrial structure in the endothelium of intact arteries, Cardiovasc. Res. 115 (2019) 1546–1556.
[43] J.G. McCormack, A.P. Halestrap, R.M. Denton, Role of calcium ions in regulation of mammalian intramitochondrial metabolism, Physiol. Rev. 70 (1990) 391–425.
[44] J. Grosskreutz, L. Van Den Bosch, B.U. Keller, Calcium dysregulation in amyotrophic lateral sclerosis, Cell Calcium 47 (2010) 165–174.
[45] M.L. Tradewell, L.A. Cooper, S. Minotti, H.D. Durham, Calcium dysregulation, mitochondrial pathology and protein aggregation in a culture model of amyotrophic lateral sclerosis: mechanistic relationship and differential sensitivity to intervention, Neurobiol. Dis. 42 (2011) 265–275.
[46] T. Makio, J. Chen, T. Simmen, ER stress as a sentinel mechanism for ER Ca(2+) homeostasis, Cell Calcium 124 (2024) 102961.
[47] X.J. Han, Y.F. Lu, S.A. Li, T. Kaitsuka, Y. Sato, K. Tomizawa, A.C. Nairn, K. Takei, H. Matsui, M. Matsushita, CaM kinase I alpha-induced phosphorylation of Drp1 regulates mitochondrial morphology, J. Cell Biol. 182 (2008) 573–585.
[48] P. Varnai, L. Hunyady, T. Balla, STIM and Orai: the long-awaited constituents of store-operated calcium entry, Trends Pharmacol. Sci. 30 (2009) 118–128.
[49] K. Wang, H. Chen, L. Cheng, J. Zhao, B. Huang, D. Wu, X. He, Y. Zhou, Y. Yuan, F. Zhou, J. Jiang, L. Chen, D. Jiang, Structure and transport mechanism of human riboflavin transporters, Nat. Commun. 16 (2025) 4078.
[50] S. Kaspar, C. Oertlin, K. Szczepanowska, A. Kukat, K. Senft, C. Lucas, S. Brodesser, M. Hatzoglou, O. Larsson, I. Topisirovic, A. Trifunovic, Adaptation to mitochondrial stress requires CHOP-directed tuning of ISR, Sci. Adv. 7 (2021).
[51] F. Rizzo, A. Ramirez, C. Compagnucci, S. Salani, V. Melzi, A. Bordoni, F. Fortunato, A. Niceforo, N. Bresolin, G.P. Comi, E. Bertini, M. Nizzardo, S. Corti, Genome-wide RNA-seq of iPSC-derived motor neurons indicates selective cytoskeletal perturbation in Brown-Vialetto disease that is partially rescued by riboflavin, Sci. Rep. 7 (2017) 46271.
[52] Y. Yao, A. Yonezawa, H. Yoshimatsu, S. Masuda, T. Katsura, K. Inui, Identification and comparative functional characterization of a new human riboflavin transporter hRFT3 expressed in the brain, J. Nutr. 140 (2010) 1220–1226.
[53] C. Marioli, V. Magliocca, S. Petrini, A. Niceforo, R. Borghi, S. Petrillo, P. La Rosa, F. Colasuonno, T. Persichini, F. Piemonte, K. Massey, M. Tartaglia, S. Moreno, E. Bertini, C. Compagnucci, Antioxidant amelioration of Riboflavin Transporter deficiency in motoneurons derived from patient-specific induced pluripotent stem cells, Int. J. Mol. Sci. 21 (2020).
[54] P. Pizzo, C. Fasolato, T. Pozzan, Dynamic properties of an inositol 1,4,5-trisphosphate- and thapsigargin-insensitive calcium pool in mammalian cell lines, J. Cell Biol. 136 (1997) 355–366.
[55] U.K. Laemmli, Cleavage of structural proteins during the assembly of the head of bacteriophage T4, Nature 227 (1970) 680–685.
[56] K. Okita, Y. Matsumura, Y. Sato, A. Okada, A. Morizane, S. Okamoto, H. Hong, M. Nakagawa, K. Tanabe, K. Tezuka, T. Shibata, T. Kunisada, M. Takahashi, J. Takahashi, H. Saji, S. Yamanaka, A more efficient method to generate integration-free human iPS cells, Nat. Methods 8 (2011) 409–412.
[57] A. Tonazzi, C. Mantovani, M. Colella, G. Terenghi, C. Indiveri, Localization of mitochondrial carnitine/acylcarnitine translocase in sensory neurons from rat dorsal root ganglia, Neurochem. Res. 38 (2013) 2535–2541.
[58] A. Chaudhry, R. Shi, D.S. Luciani, A pipeline for multidimensional confocal analysis of mitochondrial morphology, function, and dynamics in pancreatic beta-cells, Am. J. Physiol. Endocrinol. Metabol. 318 (2020) E87–E101.
[59] B. Ryder, M. Tolomeo, Z. Nochi, M. Colella, M. Barile, R.K. Olsen, M. Inbar-Feigenberg, A novel truncating FLAD1 variant, causing Multiple Acyl-CoA Dehydrogenase Deficiency (MADD) in an 8-Year-Old boy, JIMD reports 45 (2019) 37–44.
[60] Superti-Furga, G. Lackner, D. Wiedmer, T. Ingles-Prieto, A. Barbosa, B. Girardi, E. Goldmann, U. Gurtl, B. Klavins, K. Klimek, C. Lindinger, S. Lineiro-Retes, E. Muller, A.C. Onstein, S. Redinger, G. Reil, D. Sedlyarov, V. Wolf, G. Crawford, M. Everley, R. Hepworth, D. Liu, S. Noell, S. Piotrowski, M. Stanton, R. Zhang, H. Corallino, S. Faedo, A. Insidioso, M. Maresca, G. Redaelli, L. Sassone, F. Scarabottolo, L. Stucchi, M. Tarroni, P. Tremolada, S. Batoulis, H. Becker, A. Bender, E. Chang, Y.N. Ehrmann, A. Muller-Fahrnow, A. Putter, V. Zindel, D. Hamilton, B. Lenter, M. Santacruz, D. Viollet, C. Whitehurst, C. Johnsson, K. Leippe, P. Baumgarten, B. Chang, L. Ibig, Y. Pfeifer, M. Reinhardt, J. Schonbett, J. Selzer, P. Seuwen, K. Bettembourg, C. Biton, B. Czech, J. de Foucauld, H. Didier, M. Licher, T. Mikol, V. Pommereau, A. Puech, F. Yaligara, V. Edwards, A. Bongers, B.J. Heitman, L.H. Ap, I.J. Sijben, H.J. van Westen, G.J.P. Grixti, J. Kell, D. B. Mughal, F. Swainston, N. Wright-Muelas, M. Bohstedt, T. Burgess-Brown, N. Carpenter, L. Durr, K. Hansen, J. Scacioc, A. Banci, G. Colas, C. Digles, D. Ecker, G. Fuzi, B. Gamsjager, V. Grandits, M. Martini, R. Troger, F. Altermatt, P. Doucerain, C. Durrenberger, F. Manolova, V. Steck, A. L, et al., The RESOLUTE consortium: unlocking SLC transporters for drug discovery, Nat. Rev. Drug Discov. 19 (2020) 429–430.
[61] A. Gerbino, I. Maiellaro, C. Carmone, R. Caroppo, L. Debellis, M. Barile, G. Busco, M. Colella, Glucose increases extracellular [Ca2+] in rat insulinoma (INS-1E) pseudoislets as measured with Ca2+-sensitive microelectrodes, Cell Calcium 51 (2012) 393–401.
[62] M.M. Bradford, A rapid and sensitive method for the quantitation of microgram quantities of protein utilizing the principle of protein-dye binding, Anal. Biochem. 72 (1976) 248–254.
[63] A. Nisco, T.M.A. Carvalho, M. Tolomeo, D. Di Molfetta, P. Leone, M. Galluccio, M. Medina, C. Indiveri, S.J. Reshkin, R.A. Cardone, M. Barile, Increased demand for FAD synthesis in differentiated and stem pancreatic cancer cells is accomplished by modulating FLAD1 gene expression: the inhibitory effect of Chicago Sky Blue, FEBS J. 290 (2023) 4679–4694.